

Impact of pyruvic acid photolysis on acetaldehyde and peroxy radical formation in the boreal forest: Theoretical calculations and model results.

5 Philipp G. Eger¹, Luc Vereecken², Rolf Sander¹, Jan Schuladen¹, Nicolas Sobanski¹, Horst Fischer¹, Einar Karu¹, Jonathan Williams¹, Ville Vakkari^{3,4}, Tuukka Petäjä⁵, Jos Lelieveld¹, Andrea Pozzer¹ and John N. Crowley¹

¹Atmospheric Chemistry Department, Max-Planck-Institute for Chemistry, 55128-Mainz, Germany

²Institute for Energy and Climate Research: IEK-8, Forschungszentrum Juelich, 52425 Juelich, Germany

10 ³Atmospheric Composition Unit, Finnish Meteorological Institute, 00101 Helsinki, Finland

⁴Atmospheric Chemistry Research Group, Chemical Resource Beneficiation, North-West University, Potchefstroom, South Africa

⁵Institute for Atmospheric and Earth System Research (INAR) / Physics, Faculty of Science, University of Helsinki, Finland

Correspondence to: John N. Crowley (john.crowley@mpic.de) ~~Modelling the impact of gas-phase pyruvic acid on acetaldehyde and peroxy radical formation in the boreal forest~~

15 ~~Philipp G. Eger¹, Jan Schuladen¹, Nicolas Sobanski¹, Horst Fischer¹, Einar Karu¹, Jonathan Williams¹, Ville Vakkari^{2,3}, Jos Lelieveld⁴ and John N. Crowley¹~~

20 ~~¹Atmospheric Chemistry Department, Max-Planck-Institute for Chemistry, 55128 Mainz, Germany~~

~~²Atmospheric Composition Unit, Finnish Meteorological Institute, 00101 Helsinki, Finland~~

~~³Atmospheric Chemistry Research Group, Chemical Resource Beneficiation, North-West University, Potchefstroom, South Africa~~

Correspondence to: John N. Crowley (john.crowley@mpic.de)

25 **Abstract.**

Based on the first measurements of gas-phase pyruvic acid ($\text{CH}_3\text{C}(\text{O})\text{C}(\text{O})\text{OH}$) in the boreal forest, we derive effective emission rates of pyruvic acid and compare them with monoterpene emission rates over the diel cycle. Using a data-constrained box-model, we determine the impact of pyruvic acid photolysis on the formation of acetaldehyde (CH_3CHO) and the peroxy radicals $\text{CH}_3\text{C}(\text{O})\text{O}_2$, CH_2O_2 and HO_2 during an autumn (~~IBAIRN~~) and summer (~~HUMPPA~~) campaign (~~IBAIRN, 2016~~) in the boreal forest ~~at the same site.~~

30 The results are dependent on the quantum yield (ϕ) and mechanism of the photodissociation of pyruvic acid and the fate of a likely major product, methylhydroxy carbene (CH_3COH). With the box-model, we investigate two different scenarios in which we follow the present IUPAC recommendations with $\phi = 0.2$ (at 1 bar of air) and the main photolysis products (60 %) are acetaldehyde + CO_2 with 35% C-C bond fission to form HOCO and CH_3CO (scenario A). In the second scenario (B), the

35 formation of vibrationally hot CH_3COH (and CO_2) represents the main dissociation pathway at longer wavelengths (~75%) with a ~25% contribution from C-C bond fission to form HOCO and CH_3CO (at shorter wavelengths). In scenario 2 we vary ϕ between 0.2 and 1 and, based on the results of our theoretical calculations, allow the thermalised CH_3COH to react with O_2 (forming peroxy radicals) and to undergo acid-catalysed isomerisation to CH_3CHO .

When constraining the pyruvic acid to measured mixing ratios and independent of the model scenario, we find that the photolysis
40 of pyruvic acid is the dominant source of CH_3CHO during the IBairn campaign with a contribution between ~70 and 90 % to the total production rate. We find that the photolysis of pyruvic acid is also a major source of the acetylperoxy radical, with contributions varying between ~20 and 60 % dependent on the choice of ϕ and the products formed. HO_2 production rates are also enhanced, mainly via the formation of CH_3O_2 . The elevated production rates of $\text{CH}_3\text{C(O)O}_2$ and HO_2 and concentration of CH_3CHO result in significant increases in the modelled mixing ratios of $\text{CH}_3\text{C(O)OOH}$, CH_3OOH , HCHO and H_2O_2 .

~~45 The results are dependent on the photodissociation mechanism of pyruvic acid and we examine different scenarios in which the main photolysis products are either acetaldehyde or the $\text{CH}_3\text{C(O)O}_2$ radical, with different overall quantum yields. If CH_3CHO is taken to be the main product (as presently recommended by evaluation panels) we find that pyruvic acid photolysis can be a dominant source of this aldehyde in the boreal forest with a contribution of 79 % (IBairn) and 94 % (HUMPPA) and may help explain the high acetaldehyde levels observed during HUMPPA. On the other hand, if photolysis leads mainly
50 to the formation of radicals, the emission of pyruvic acid has a profound impact on the rates of formation of peroxy radicals (with a contribution of ~20–50 %) and shifts the onset of radical production to earlier in the morning when actinic flux is dominated by wavelengths that are too long to initiate efficient ozone photolysis but which are absorbed by pyruvic acid.~~

1 Introduction

55 Organic acids play a crucial role in tropospheric chemistry, impacting secondary organic aerosol formation, air quality and climate (Kanakidou et al., 2005; Hallquist et al., 2009). Pyruvic acid ($\text{CH}_3\text{C(O)C(O)OH}$), an organic acid that is central in plant metabolism as part of the Krebs cycle (Walker, 1962), is found in tropospheric air in the gas phase as well as in the aerosol phase, especially in the boundary layer ~~of over~~ vegetated regions. Gas-phase mixing ratios ranging from a few to several hundred parts per trillion (pptv) have been reported in various locations around the world, including the tropical rain
60 forest, boreal forest, rural areas with temperate forest, and regions influenced by urban outflow. A recent overview of existing measurements of gas-phase pyruvic acid is given by Eger et al. (2020).

A ~~known major~~ source of pyruvic acid is ~~understood to be~~ the photo-oxidation of isoprene, via the ozonolysis of methyl vinyl ketone and subsequent hydrolysis of the Criegee intermediates (Jacob and Wofsy, 1988; Grosjean et al., 1993; Paulot et al., 2009). Further potential sources are the photolysis of methylglyoxal (Raber and Moortgat, 1995), the gas-phase photo-
65 oxidation of aromatics in the presence of NO_x (Grosjean, 1984; Praplan et al., 2014), the aqueous-phase oxidation of methylglyoxal (Stefan and Bolton, 1999) and reactions taking place within biomass burning plumes (Andreae et al., 1987;

Helas et al., 1992). In addition, pyruvic acid has been reported to be directly emitted from vegetation (Talbot et al., 1990; Jardine et al., 2010a; Jardine et al., 2010b; Eger et al., 2020). Compared to acetic acid, the presence of a second (non-acidic) carbonyl group imparts on pyruvic acid an absorption spectrum that extends from ultraviolet to visible wavelengths (see Fig. 1) and photolysis is a major sink of pyruvic acid in the boundary layer, with deposition and heterogeneous uptake to the aerosol phase also contributing to its removal. Photolysis of pyruvic acid in air results in a number of different radical and stable products (see Fig. 1), the major ones are expected to be ~~being~~ acetaldehyde, HO₂ and CH₃C(O)O₂ (more details are presented in Sect. 2.12.1). These products can have a significant impact on tropospheric chemistry, e.g. via the formation of peroxyacetyl nitrate (PAN), peracetic acid (PAA) and formaldehyde (HCHO).

Global models have recently revealed discrepancies between simulated and measured acetaldehyde concentrations (Millet et al., 2010; Wang et al., 2019; Wang et al., 2020). Wang et al. (2020) reported CH₃CHO mixing ratios that were up to a factor of 10 higher than ~~predicted by a~~ global chemistry-transport model (EMAC) ~~results~~ in the marine boundary layer around the Arabian Peninsula, implying missing sources of CH₃CHO in remote and polluted regions. Wang et al. (2019) also found that models systematically underestimate CH₃CHO compared to observations ~~in the remote troposphere~~, implying a missing source of acetaldehyde ~~in the remote troposphere~~. This finding was supported by the simultaneous measurement of PAA (which is formed e.g. via the degradation of acetaldehyde in remote environments) ~~This finding was supported by the simultaneous measurement of PAA (for which acetaldehyde is a precursor in remote environments) and by the~~ with the organic aerosol source of CH₃CHO ~~also being~~ insufficient to explain the results. Instead, Wang et al. (2019) suggested that CH₃CHO arises from the degradation of gas-phase organic compounds. Pyruvic acid, among other organic acids in the gas and aerosol phase, might be one of the compounds that ~~transport and can be converted~~ ~~release to~~ acetaldehyde to the remote troposphere and its integration into global models might contribute to resolve discrepancies, especially in forested regions.

Generally, field measurements as well as modelling and laboratory-based kinetic studies on pyruvic acid are limited and its impact on atmospheric chemistry is still poorly understood. In this study we highlight the potential role of pyruvic acid in the boreal forest, one of the largest terrestrial biomes on Earth. ~~For this, we use data from a measurement campaign in 2016~~ (IBAIRN, Influence of Biosphere–Atmosphere Interactions on the Reactive Nitrogen budget).

1.1 The photolysis of pyruvic acid: Quantum yields and products

Because its reaction with OH is slow ($k_{\text{OH+pyruvic acid}} = 1.2 \times 10^{-13} \text{ cm}^3 \text{ molecule}^{-1} \text{ s}^{-1}$ at 298 K, (Mellouki and Mu, 2003)), photolysis and dry deposition are the dominant loss terms for gas-phase pyruvic acid. Heterogeneous uptake to atmospheric aerosols is also calculated to be inefficient during the IBAIRN campaign in the boreal forest (see below), where particle surface area densities were of the order of $2 \times 10^{-7} \text{ cm}^2 \text{ cm}^{-3}$ and the particles contained a large organic fraction (Liebmann et al., 2019) that is likely to reduce the uptake coefficient compared to that measured for pure aqueous particles ($\gamma = 0.06$, Eugene et al. (2018)).

The photodissociation of pyruvic acid at actinic wavelengths is not well understood. According to the most recent IUPAC evaluation (IUPAC, 2020), which considers experimental data until 2017, the three thermodynamically accessible photolysis channels are:



IUPAC recommend a photodissociation quantum yield (ϕ) of 0.2 at 1 bar pressure (i.e. for boundary layer conditions) with branching ratios of 0.6, 0.05 and 0.35 for reactions R1, R2 and R3, respectively, which implicitly assumes that the initially formed carbene ($\text{CH}_3\text{COH}^\#$) immediately isomerises to acetaldehyde. The radical products of reaction R3 (CH_3CO and HOCO) react rapidly in air to form peroxy radicals (R4, R5).



The formation of methylhydroxy carbene (CH_3COH) as an intermediate in pyruvic acid photolysis has been postulated for many years (Vesley and Leermakers, 1964; Yamamoto and Back, 1985). Schreiner et al. (2011), observed isomerisation of singlet CH_3COH to acetaldehyde in an Ar matrix at 11 K; their high level theoretical analysis revealing high barriers for isomerisation, where H-atom tunnelling through the energy barrier led to a lifetime of about 1 hour at 11 K, favouring the formation of acetaldehyde over that of vinyl alcohol. Only very recently has CH_3COH been detected experimentally as a product of pyruvic acid photolysis in the gas-phase (Samanta et al., 2021) and its unimolecular isomerisation to both CH_3CHO and $\text{CH}_2=\text{CHOH}$ confirmed to be efficient at the experimental pressure of a few mbar of helium. Indeed, Samanta et al. (2021) show that, at a photolysis wavelength of 351 nm (close to the maximum cross-section of pyruvic acid) formation of an energy-rich carbene ($\text{CH}_3\text{COH}^\#$) and CO_2 (R6) is essentially the only product channel operating. CH_3CHO and $\text{CH}_2=\text{CHOH}$ were formed subsequently (at ~ 2:1 ratio favouring CH_3CHO) in the unimolecular isomerisation of $\text{CH}_3\text{COH}^\#$ (R7, R8).



Samanta et al. (2021) suggest that, at ambient pressures, a significant fraction of the energised, nascent carbene will be deactivated by collisions with air (R9) and the thermalised carbene (CH_3COH), which can no longer rapidly overcome the barriers to isomerisation, may react with oxygen or water vapour (Reed Harris et al., 2016; Reed Harris et al., 2017b; Eger et al., 2020; Samanta et al., 2021) (R10, R11).



130 As summarised by IUPAC (2020), there have been many experimental studies deriving primary photodissociation quantum
yields and product yields following the photolysis of pyruvic acid. The studies which were carried out at atmospherically
relevant wavelengths (i.e. within the ~300 - 400 nm absorption band) are listed in Table S1. The experiments were carried out
at different pressures of various bath gases and at different wavelengths and at different concentrations of pyruvic acid, all of
which appear to play a role in determining the products formed. Table S1 shows that CO₂ is formed at a yield of close to 100%
135 whereas the yield of CH₃CHO is highly variable. CH₂=CHOH has been detected both at a few Torr of Helium (Samanta et al.,
2021) and at 1bar of air (Calvert et al., 2011). Other end-products observed during the photolysis of pyruvic acid in 1 bar of
air include acetic acid (Calvert et al., 2011; Reed Harris et al., 2016; Reed Harris et al., 2017b) and PAN (Grosjean, 1983;
Berges and Warneck, 1992) when NO₂ was present, which together provide evidence for the formation of the acetyl peroxy
radical (CH₃C(O)O₂), and thus CH₃CO, e.g., in reaction R3 and R4 when sunlight or solar-simulating light sources are used.
140 Further secondary products (resulting e.g. from the further reactions of CH₃CHO) such as HCHO and CH₃OH have also been
observed at pressures close to 1 bar (Grosjean, 1983; Calvert et al., 2011; Reed Harris et al., 2016; Reed Harris et al., 2017a).
While the Norrish type-1 process (C-C bond fission) forming CH₃CO and HOCO appears to be unimportant at 351 nm
(Samanta et al., 2021), it may be favoured at wavelengths < 340 nm (Chang et al., 2014). This is illustrated in Fig. 1 where we
present the wavelength resolved photolysis rate constants across the UV-absorption spectrum of pyruvic acid (assuming an
145 overall photolysis quantum yield of 1, and absorption cross-sections recommended by IUPAC). The wavelength resolved
actinic flux was calculated for the IBairn measurement site on the 16.09.2016 using the Tropospheric Ultraviolet and Visible
Radiation model (TUV, https://www.acom.ucar.edu/Models/TUV/Interactive_TUV/). Integration of the J-values at
wavelengths < 340 nm, indicate that (at local noon) ≈ 25% of pyruvic acid dissociation occurs at these shorter wavelengths.

150 ~~2 Experimental data and box model description~~Methods

The goal of this study is to ~~quantify-evaluate~~ the impact of pyruvic acid on acetaldehyde and radical formation rates in the
boreal forest by using a data-constrained, chemical box-model. For this purpose we make use of experimental data from ~~two~~
~~field-studies~~a field study, which ~~were-was both~~ performed in the Finish boreal forest at the “Station for Measuring Forest
Ecosystem-Atmosphere Relations II” (SMEAR II) in Hyytiälä (61.846 °N, 24.295 °E, 180 m above sea level, see Hari and
155 Kulmala (2005)), an area that is characterised by large emission rates of biogenics (mainly monoterpenes) and low NO_x
concentrations ~~an area that is mainly characterised by large biogenic (monoterpene dominated) emissions and low NO_x
concentrations~~ ~~{!!! INVALID CITATION !!! {Williams`, 2011`#3720`; Rinne`, 2000`#5329}, #0; Aalto, 2015 #5330; Fischer,
2021 #5331; Williams, 2011 #3720}~~. An overview of the instruments used to measure trace gases and other parameters relevant
for this study is presented in Table S1 of the supplementary information. (Rinne et al., 2000; Williams et al., 2011; Aalto et al.,
160 2015; Fischer et al., 2021).

The variability in the reported photodissociation quantum yield and product distributions (IUPAC, 2021) suggests that pyruvic acid photodissociation is not yet fully understood. In addition, the fate of the potentially dominant carbene product (Samanta et al., 2021) is unknown. (Samanta et al., 2021) Therefore, in order to better constrain the fate of CH₃COH in the atmosphere, quantum chemical calculations were undertaken to characterise its likely atmospheric reactions, for which experimental data does not exist.

2.1. The IBAIRN and HUMPPA campaigns

The IBAIRN campaign (~~Influence of Biosphere–Atmosphere Interactions on the Reactive Nitrogen budget~~) took place in September 2016, during the summer–autumn transition, and was characterised by frequent temperature inversions near ground level during night-time (Liebmann et al., 2018a), which led to the accumulation of nocturnally emitted trace gases from vegetation. A detailed description of the campaign and the instruments ~~deployed~~ ~~setup~~ can be found elsewhere (Liebmann et al., 2018a; Eger et al., 2020). A summary (with details of detection limit etc.) is provided in Table S2. Briefly, pyruvic acid was measured by a chemical ionisation quadrupole mass spectrometer ~~with a detection limit (LOD) (10 s, 2σ) of 15 pptv~~ (Eger et al., 2020), ~~the~~ ~~–~~the sum of monoterpenes (henceforth referred to as MT) was measured by a PTR-ToF-MS and single monoterpenes were monitored by a GC-AED ~~–, described in detail by–~~ (Liebmann et al., 2018a). Despite some discrepancies related to instrument location and inhomogeneity in terpene emissions within the forest, both instruments were in reasonably good agreement throughout the campaign. Since ~~we require~~ a high temporal resolution is preferable for our simulation, we have used the PTR-ToF-MS dataset. NO and NO₂ were measured by chemiluminescence detector and cavity ring down spectrometer (Sobanski et al., 2016; Liebmann et al., 2018b), ozone was measured by optical absorption ~~{Eger, 2020 #5119}~~ and CO by Quantum-cascade-Laser absorption spectroscopy (Eger et al., 2020). Formic and acetic acid as well as methyl-ethyl-ketone (MEK) and methyl-vinyl-ketone (MVK) were taken from the continuous PTRMS measurements at the site at heights between 42 and 336 m. Photolysis rate coefficients were derived using actinic flux measurements from a spectral radiometer (METCON GmbH) ~~Photolysis rate coefficients (J_{pyr} , J_{NO_2} , $J_{\text{O}(\text{1D})}$ and J_{HClO}) were derived using actinic flux measurements from a spectral radiometer~~ (METCON GmbH) and evaluated cross sections and quantum yields (Burkholder et al., 2015). Mixing layer (MXL) heights were derived by combining in-situ measurements made by a scanning Doppler lidar (Hellén et al., 2018) with results from the ECMWF ERA-Interim reanalysis (Dee et al., 2011) with a spatial resolution of ~80 km. Since the lidar was unable to resolve MXL heights < 60 m (as regularly experienced during nocturnal inversions), all values below this threshold have been set to 60 m, representing an upper limit.

2.2 Theoretical analysis of the fate of singlet methylhydroxy carbene, CH₃COH

We investigated the reactions of CH₃COH theoretically under atmospheric conditions, examining its unimolecular reactions, and bimolecular reactions with O₂, H₂O and HC(O)OH, where the latter is representative of carboxylic acids. The reaction with pyruvic acid itself is also briefly explored. The rovibrational characteristics and energetics of all critical points on the

potential energy surface were characterized at the CCSD(T)/aug-cc-pVTZ//M06-2X-D3/aug-cc-pVTZ level of theory with a wavenumber scaling factor of 0.971 (Zhao and Truhlar, 2008; Dunning, 1989; Purvis and Bartlett, 1982; Grimme et al., 2011; Database of Frequency Scale Factors for Electronic Model Chemistries (Version 4); Alecu et al., 2010). This method compares favourably with the more rigorous focal point analysis of Schreiner et al. (2011), with energy differences in the singlet state unimolecular chemistry of less than 0.7 kcal mol⁻¹, indicating that the method is reliable for kinetic predictions under atmospheric temperatures. Where necessary, broken symmetry SCF calculations were used to describe singlet biradicals (Noodleman, 1981), and IRC calculations were used to verify the pathways. For reactants, products and transition states we exhaustively characterized all conformers; for complexes we only characterized those directly connecting to a transition state. All quantum chemical calculations were performed using the Gaussian-16 program suite (Frisch et al., 2016). The quantum chemical data was then used to calculate high-pressure rate coefficients for reactions over a saddle point using multi-conformer transition state theory (MC-TST) calculations (Vereecken and Peeters, 2003), under a rigid rotor harmonic oscillator approximation. Tunnelling corrections are performed assuming an asymmetric Eckart barrier (Eckart, 1930; Johnston and Heicklen, 1962). Most reactions have high energy barriers, and the presence of pre- and post-reaction complexes has negligible influence on the reaction rate. For barrierless reactions, typically complexation reactions, we assume the reaction rate is close to the collision limit unless indicated otherwise.

~~The summertime boreal forest field measurement intensive HUMPPA-COPEC took place at the same location in July and August 2010 and was characterised by unusually warm temperatures for this time of the year with exceptionally large emissions from the biosphere. A detailed description of the campaign and meteorological situation can be found in Williams et al. (2011). Insights into HO_x and RO_x chemistry are presented by Crowley et al. (2018) who suggested that di-carbonyl compounds, including pyruvic acid, could help explain the high production rates of radicals necessary to explain the observations of H₂O₂ and PAA, especially during periods when the measurement site was impacted by biomass burning in Russia.~~

2.32 Box model description

~~The box model was developed with the goal of simulating the impact of pyruvic acid photolysis on formation rates of OH, HO₂, CH₃C(O)O₂, CH₃CHO, CH₃O₂, HCHO and CH₂OOH over several diel cycles during the two field campaigns in the Finish boreal forest described above. We have used the CAABA/MECCA atmospheric chemistry box model to numerically simulate the impact of pyruvic acid photolysis on the formation of radicals and CH₃CHO over the diel cycle during the IBairn campaign. Our study is based on model version 4.4.2, with updated reactions related to pyruvic acid in which two different scenarios were investigated (see section 3.3) in order to examine the sensitivity of the model output to e.g. photolysis quantum yields and products.~~

The chemical mechanism used in this study contains >600 gas-phase species and ~2000 gas-phase reactions and photolysis steps. In addition to the basic ozone, HO_x and NO_x chemistry, the mechanism contains the detailed "Mainz Organic Mechanism" (MOM) for non-methane hydrocarbons (NMHC), isoprene, terpenes, and aromatics. MOM is derived from a reduced version of the Master Chemical Mechanism (MCM). Full details about CAABA/MECCA and MOM are available in

Sander et al. (2019). Photolysis reactions are calculated for a latitude of 62 °N. A complete reaction scheme and source of rate coefficients can be found in the data archive (see “data availability”).

230 Several parameters (temperature, pressure, relative humidity), and trace-gas concentrations (pyruvic acid, O₃, NO, NO₂, PAN, CO, monoterpenes, formic and acetic acid, methyl-ethyl-ketone (MEK), methyl-vinyl-ketone (MVK)) as well as the photolysis
rate constants of various trace-gases were constrained to values measured during the IBAIRN campaign. The atmospheric methane mixing ratio was set to a constant value of 1.8 ppmv. Non-methane alkanes, the degradation of which represents ~
30–45 % of the acetaldehyde source globally (Millet et al., 2010) were constrained to 1000 pptv of ethane, 250 pptv of propane and 150 pptv of n-butane, as found in similar environments in Finland (Hakola et al., 2006; Hellén et al., 2015). The mixing
235 ratio of PAN, which is generally the most abundant of peroxy acetyl nitrates (PNs), was calculated from a measurement of the sum of peroxy nitrates whereby [PAN] = 0.9 × Σ[PNs] (estimation based on observations by e.g. Shepson et al. (1992b),
Roberts et al. (2004) and Roiger et al. (2011)). The model-generated, averaged OH concentration through the diel cycle was in good agreement (within ~20%) with that calculated from the correlation of ground-level OH measurements with UVB
radiation intensity at the Hyytiälä site (with [OH] = 5.62 × 10⁵ [UVB]^{0.62} molecule cm⁻³ when UVB is in units of W m⁻² (Petäjä
et al., 2009; Hellén et al., 2018)) but showed more variability resulting from changes in NO mixing ratios and the conversion
240 of HO₂ to OH.

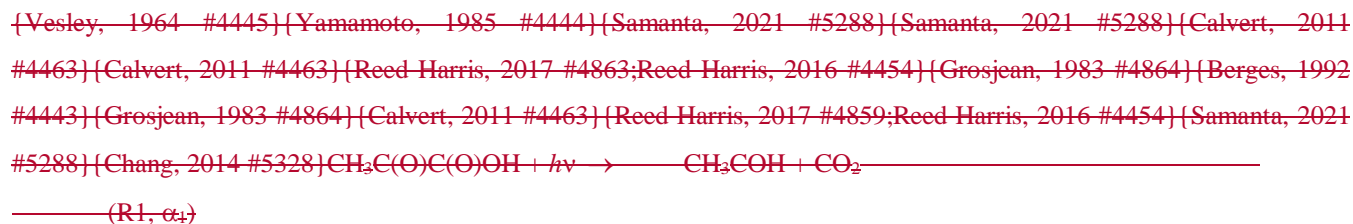
~~In all model runs, the parameters directly constrained by the observations were the temperature, pressure, relative humidity (RH), the gas-phase concentrations of O₃, NO, NO₂, PAN, CO and monoterpenes, as well as the photolysis rate constants $J_{O(1D)}$, J_{NO_2} , J_{HCHO} , J_{HONO} and J_{pyr} . Depending on the campaign (IBAIRN or HUMPPA), other parameters were additionally constrained (see Sect. 2.2.2 and 2.2.3). A complete reaction scheme is listed in Table S2 of the Supplement. Rate coefficients
245 were taken from the IUPAC evaluations (IUPAC, 2020). The atmospheric methane concentration was set to a constant value of 1.8 ppmv. Non-methane alkanes, the degradation of which represents ~30–45 % of the acetaldehyde source globally (Millet
et al., 2010) were constrained to 1000 pptv of ethane, 250 pptv of propane and 150 pptv of n-butane, as found in similar environments in Finland (Hakola et al., 2006; Hellén et al., 2015).~~

~~For the box model, programmed in FACSIMILE code (Curtis and Sweetenham, 1987), three different scenarios were
250 investigated, in which the pyruvic acid chemistry listed in Table S2 was modified (see below) in order to examine the sensitivity of the model output to photolysis quantum yields. The box model simulated the field data at 10-min temporal
resolution.~~

~~2.2.1 Pyruvic acid loss rate and model scenarios~~

~~Photolysis and dry deposition are considered the dominant loss terms for gas-phase pyruvic acid, as reaction with OH is slow
255 (1.2×10^{-13} cm³ molecule⁻¹ s⁻¹ at 298 K) (Mellouki and Mu, 2003). Heterogeneous uptake to atmospheric aerosols is also calculated to be inefficient at this site, where particle surface area densities were of the order of 2×10^{-7} cm² cm⁻³ and the
particles contained a large organic fraction (Liebmann et al., 2019) that is likely to reduce the uptake coefficient compared to that measured for purely aqueous particles ($\gamma = 0.06$, Eugene et al. (2018)).~~

In Fig. 1 we present the wavelength-resolved photolysis rates across the UV-absorption spectrum of pyruvic acid (assuming the overall photolysis quantum yield is 0.2) and a scheme showing possible routes to formation of acetaldehyde and radicals following its photolysis. The three most important photolysis channels are:



where α_i are branching ratios with $\alpha_1 + \alpha_2 + \alpha_3 = 1$.

CH_3CO and HOCO react rapidly in air to form peroxy radicals:



The methylhydroxycarbene product of R1 (CH_3COH) is an unstable intermediate which can rearrange to form CH_3CHO (R6) with branching ratio β or react with O_2 to form HO_2 and CH_3CO (branching ratio $1 - \beta$), which via R4, results in formation of $\text{CH}_3\text{C(O)O}_2$.



The methylhydroxycarbene product of R1 (CH_3COH) is an unstable intermediate which can rearrange to form CH_3CHO (R6) with branching ratio β or react with O_2 to form HO_2 and CH_3CO (branching ratio $1 - \beta$), which via R4, results in formation of $\text{CH}_3\text{C(O)O}_2$.

The quantum yield of acetaldehyde formation (ϕ_1) is thus equal to $\phi\alpha_1\beta$, where ϕ is the overall quantum yield. The quantum yield of formation of $\text{CH}_3\text{CO}_3 + \text{HO}_2$ (via R1/R7 and R2) is $\phi\alpha_2 + \phi\alpha_1(1 - \beta)$. Direct formation of $\text{CH}_3\text{C(O)OH}$ in R3 has a quantum yield of $\phi\alpha_3$.

For the calculation of the pyruvic acid photolysis rate constant (J_{pyr}) and photolysis products we used different scenarios A–C that reflect the large variability in quantum yields and branching ratios reported in the literature. They are outlined in the following and summarised in Table 1 along with the dominant photolysis products in air. In scenario A, which represents a reference for the other scenarios, we assumed that the overall quantum yield for pyruvic acid photolysis (ϕ) is zero. As its reaction with OH is slow, setting J_{pyr} to zero effectively removes any contribution of pyruvic acid to acetaldehyde or radical generation. In scenario B we used pyruvic acid cross sections and quantum yields according to the UPAC recommendations (IUPAC, 2020), with an overall quantum yield of $\phi = 0.2$ and branching ratios $\alpha_1 = 0.6$, $\alpha_2 = 0.35$ and $\alpha_3 = 0.05$, favouring the formation of acetaldehyde. Scenario C is based on the quantum yields reported by Reed Harris et al. (2017) who suggest $\phi =$

0.84 with $\alpha_4 = 1$ and $\beta = 0.05$, i.e. only two relevant product channels forming mainly $\text{CH}_2\text{CO}_2 + \text{HO}_2$ (95%) and only low amounts of CH_2CHO (5%). The comparison of scenarios B and C illustrates the sensitivity of the model output to the chosen quantum yields and branching ratios. The plausibility of the scenarios is tested by comparing the results of our model runs with observations of acetaldehyde and PAA during HUMPPA.

The deposition rate of pyruvic acid was calculated from $k_{\text{dep}} = v_{\text{dep}} h_{\text{MXL}}^{-1}$ during day and $k_{\text{dep}} = 2 v_{\text{dep}} h_{\text{MXL}}^{-1}$ during night (Shepson et al., 1992a), with the transition following the diel variation in the mixing layer height h_{MXL} (see Fig. S1 in the Supplement). Further, as the two trace gases have similar solubilities, we assumed that the deposition velocity of pyruvic acid is equal to that of H_2O_2 , so that $v_{\text{dep}} = 8.4 \text{ cm s}^{-1}$ during day and $v_{\text{dep}} = 0.8 \text{ cm s}^{-1}$ during night, as derived by Crowley et al. (2018) for the same site. This resulted in a minimum dry deposition loss rate constant of $k_{\text{dep}} = 0.9 \times 10^{-4} \text{ s}^{-1}$ during day and a maximum of $k_{\text{dep}} = 1.8 \times 10^{-4} \text{ s}^{-1}$ during night.

2.2.2 IB AIRN simulation

The simulation was initiated on 05.09.2016 but we analysed the model output only in the period 09–21.09.2016, as high-resolution MT data was not available for the first campaign days. In addition to the parameters generally constrained in all model runs (see above), for IB AIRN the concentration of pyruvic acid was determined by the observations. The concentration of PAN, which is generally the most abundant of peroxy acetyl nitrates (PNs), was calculated from $[\text{PAN}] = 0.9 \times \Sigma[\text{PNs}]$ (estimation based on observations by e.g. Shepson et al. (1992b), Roberts et al. (2004) and Roiger et al. (2011)). OH was calculated from the correlation of ground level OH measurements with UVB radiation intensity at the Hyytiälä site (Petäjä et al., 2009; Hellén et al., 2018) with $[\text{OH}] = 5.62 \times 10^5 [\text{UVB}]^{0.62} \text{ molecule cm}^{-3}$ when UVB is in units of W m^{-2} .

We added a constant value of 1.5 s^{-1} (accounting for unmeasured oxygenated VOCs) to the total OH reactivity (R_{OH}), so that the simulated OH concentration approximately matched the OH concentration derived from the UVB measurement.

2.2.3 HUMPPA simulation

The simulation was initiated on 14.07.2010, the output was only used from 21.07.–08.08.2010 due to missing PAN data at the beginning of the campaign. In addition to the parameters generally constrained in all model runs (listed above), for HUMPPA the concentrations of HCHO, HONO and CH_2CHO were determined by the observations. However, due to a lack of experimental data, we estimated the pyruvic acid concentration based on measured MT mixing ratios and the relationship between pyruvic acid and MT emission rates derived from the IB AIRN analysis (which is discussed later in Sect. 3.1). During HUMPPA, the site was impacted by a biomass burning plume on two occasions (26.07.–30.07.2010 and 07.08.–09.08.2010) and levels of CH_3CN , CO, PAN, H_2O_2 , PAA and several oxidised organics were considerably enhanced over normal conditions. We present results both including and excluding the biomass burning periods.

3 Results and discussion

In the following, we analyse in-situ measurements of pyruvic acid to derive emission rates, present the results of the theoretical calculations of the fate of CH₃OH and discuss the box-model output for the IBAIRN campaign with a focus on pyruvic acid emission rates and its impact on acetaldehyde and radical chemistry in the boundary layer of the boreal forest. ~~In the following, we discuss the model output for the IBAIRN and HUMPPA campaigns with a focus on pyruvic acid emission rates and its impact on acetaldehyde and radical chemistry in the boundary layer of the boreal forest.~~

3.1 ~~Autumn campaign (IBAIRN):~~ Pyruvic acid emission rate relative to monoterpenes during IBAIRN

In order to ~~quantify~~ derive the pyruvic acid emission rate (E_{pyr}) during IBAIRN we assume that only photolysis and dry deposition contribute significantly to its overall loss rate (~~Sect. 2.2.1~~) and that pyruvic acid is in steady-state. The latter assumption is reasonable as its mean lifetime was (2 ± 0.5) hours. ~~h (for scenario B; shortest at night) and changes in the mixing ratio could reliably be reproduced by the simulation.~~ Due to a homogeneous fetch at the measurement site we can neglect transport processes and E_{pyr} is defined by Eq. (1), where $[\text{pyr}]_{\text{ss}}$ is the measured concentration, J_{pyr} is the photolysis rate constant of pyruvic acid, k_{dep} is the first-order loss rate constant for its dry deposition, and h_{MXL} is the well-mixed boundary layer height.

$$E_{\text{pyr}} = [\text{pyr}]_{\text{ss}} (J_{\text{pyr}} + k_{\text{dep}}) h_{\text{MXL}} \quad (1)$$

E_{pyr} is effectively an emission rate normalised to the MXL height (h_{MXL}) and has units of pptv s⁻¹ m. As the photolysis is a substantial fraction of the overall losses of CH₃C(O)C(O)OH, the choice of quantum yield ϕ (~~scenarios A, B and C~~) directly impacts the calculated emission rate.

The deposition rate of pyruvic acid was calculated from $k_{\text{dep}} = v_{\text{dep}} h_{\text{MXL}}^{-1}$ during day and $k_{\text{dep}} = 2 v_{\text{dep}} h_{\text{MXL}}^{-1}$ during night (Shepson et al., 1992a), with the transition following the diel variation in the mixing layer height h_{MXL} (see Fig. S1 in the Supplement). Further, as pyruvic acid and H₂O₂ have similar solubilities, we assumed that their deposition velocities are equal, so that $v_{\text{dep}} = 8.4 \text{ cm s}^{-1}$ during day and $v_{\text{dep}} = 0.8 \text{ cm s}^{-1}$ during night, as derived by Crowley et al. (2018) for the same site. This resulted in a minimum dry-deposition loss rate constant of $k_{\text{dep}} = 0.9 \times 10^{-4} \text{ s}^{-1}$ during day and a maximum of $k_{\text{dep}} = 1.8 \times 10^{-4} \text{ s}^{-1}$ during night.

The same calculation is performed for the monoterpenes (E_{MT}) over the same period (and thus for the same MXL height). We note that h_{MXL} controls not only the value of k_{dep} but also directly affects the mixing ratios of both MTs and pyruvic acid for a given emission rate. The relative emission rate ($E_{\text{pyr}}/E_{\text{MT}}$) can be calculated from Eq. (2) where terms in square brackets are concentrations.

$$\frac{E_{\text{pyr}}}{E_{\text{MT}}} = \frac{[\text{pyr}]_{\text{ss}} (J_{\text{pyr}} + k_{\text{dep}})}{[\text{MT}]_{\text{ss}} (k_{\text{OH}}[\text{OH}] + k_{\text{NO}_3}[\text{NO}_3] + k_{\text{O}_3}[\text{O}_3])} \quad (2)$$

In the denominator, k_{OH} , k_{NO_3} and k_{O_3} are rate coefficients for reaction of monoterpenes with OH, NO₃ and O₃, respectively.

As we do not have GC data at high time resolution, an effective rate coefficient for loss of the monoterpenes was derived from the ~~An average lifetime of MT of (4 ± 2) h (largest at night), resulting from reactions with OH, NO₃ and O₃ (see Table S2),~~

was calculated from the mean MT composition as measured by GC-AED (49 % α -pinene, 13 % β -pinene, 27 % Δ -carene (sum of 2-carene and 3-carene), 3 % Δ -limonene and 8 % camphene) and the corresponding rate coefficients (Perring et al., 2013; Gaona-Colman et al., 2017; IUPAC, 2020). This will introduce significant uncertainty (factor ~ 2) into the calculation of the MT emission rates. Further uncertainty arises from the (Perring et al., 2013; Gaona-Colman et al., 2017; IUPAC, 2020). Note that the calculated emission rates are subject to substantial uncertainties arising from the measurement of pyruvic acid, Σ MT, OH, O₃, NO₃, h_{MXL} and J_{pyr} . In particular, the results are very sensitive to the estimated deposition velocity (v_{dep}) of pyruvic acid which is an estimate based on the deposition velocity of H₂O₂ which itself has an uncertainty of ~ 90 % (Fischer et al., 2019). Further, our calculations are based on the assumption that the sources for of pyruvic acid and MT emissions are evenly distributed and measurements made at ~ 8.5 m above the ground are representative of the entire boundary layer (i.e. that the boundary layer is well-mixed, including the very shallow boundary layer at night). A gradient in pyruvic acid mixing ratios at night cannot be ruled out, which would impact on our results. We estimate that the emission ratio ($E_{\text{pyr}} / E_{\text{MT}}$) in Eq. (2) is associated with an overall uncertainty of a factor ~ 32 notwithstanding the use of different quantum yields (and thus J -values) for pyruvic acid photolysis.-

A time series of pyruvic acid and MT mixing ratios along with the MXL height height (h_{MXL}) derived from a lidar measurement and from the ERA-Interim re-analysis is shown in Fig. S2 of the Supplementary Information. Whereas both MXL height datasets agree very well during the night when the MXL is shallow (usually < 100 m), the lidar data is on average a factor of ~ 2 lower during day and characterised by a much higher variability. For the derivation of the diel profile of h_{MXL} (Fig. S1) we took an average of both datasets. The diel variation displayed in Fig. S2, with the highest MT mixing ratios at night, is characteristic for this boreal forest site and has been observed in earlier studies (Hellén et al., 2018).

In the following, we focus on the mean, diel profiles of E_{pyr} , E_{MT} , $J\text{-NO}_2$, T and h_{MXL} for the IBAIRN campaign, which are presented in Fig. 2. A plot showing the variability of the MT and pyruvic acid mixing ratios over the same period was previously reported (see Fig. 3 of Eger et al. (2020)).

During September, the emission rate of pyruvic acid (E_{pyr}) reaches its maximum a few hours after solar noon when the temperature peaks, similar to E_{MT} . However, the amplitude of the day-to-night difference in E_{pyr} is a factor of ~ 3 smaller than observed for E_{MT} . This could indicate that pyruvic acid emissions are less temperature-dependent than MT emissions (see below) and that other environmental factors might additionally play a role at this time of year.

The emission rates of the MTs derived as described above show a large day-night variation with a factor ~ 20 larger values around noontime compared to midnight. This is significantly larger than the expected variation (factor 2–3) based on the average noon-to-midnight temperature difference of 10 K and the parameterisation of Guenther et al. (1993) whereby $E_{\text{MT}} \propto \exp(\beta(T - 297 \text{ K}))$ with $\beta = 0.1 \text{ K}^{-1}$ (which is in line in with the empirical value of $\beta = 0.12 \text{ K}^{-1}$ that was derived for this site in September by Hellén et al. (2018)). One potential reason for this discrepancy may be related to emissions in autumn from fresh leaf litter that significantly contribute to the observed mixing ratios (Hellén et al., 2018) and that the assumption of evenly distributed sources and a well-mixed boundary layer is not necessarily valid during night, especially during strong temperature inversions.

Fig. S3 in the Supplement shows that the daytime emission of pyruvic acid relative to MT ($E_{\text{pyr}}/E_{\text{MT}}$) varies by a factor of ~ 2 , depending on the chosen scenario, whereas the nighttime emission ratio is only dependent on the deposition velocity of pyruvic acid. For further analysis we ~~adopt a quantum yield of 0.2 focus on the results from scenario B, using presently recommended photochemical parameters for pyruvic acid~~ (IUPAC, 2020). On average ($E_{\text{pyr}}/E_{\text{MT}}$) ~ 0.6 with a minimum value of ~ 0.3 in the evening and a maximum value of ~ 1 in the early morning, indicating elevated pyruvic acid emissions relative to MT at night. To derive a T -dependent expression from the diurnal profile of the emission factor, we fit an exponential function to the plot of temperature versus $E_{\text{pyr}}/E_{\text{MT}}$ (Fig. S4), yielding:

$$E_{\text{pyr}} = \left[0.28 + 3.17 \times \exp\left(\frac{273-T}{4.24}\right) \right] \times E_{\text{MT}} \quad (3)$$

We note that (like the values of E_{pyr}) the temperature dependence derived is strongly influenced by the diel variation of the MXL height and thus carries significant uncertainty and may not be transferable to other locations or even times of the year.

As our measurements of pyruvic acid ~~in the boreal forest~~ are the first to have been made ~~in the boreal forest~~, we cannot compare our relative emission ratio ($E_{\text{pyr}}/E_{\text{MT}}$) with previous measurements in ~~a similar the boreal~~ environment. Instead, where possible, we derive the emission ratio from measurements of MTs, isoprene and pyruvic acid in warmer climates.

Jardine et al. (2010b) performed measurements in an enclosed (glass dome) tropical forest biome at Biosphere 2 in Arizona, US, where they found maximum ~~concentrations-mixing ratios~~ of 120 ppbv isoprene, 6 ppbv monoterpenes and 15 ppbv pyruvic acid.

As the glass dome absorbed actinic wavelengths and prevented active photochemistry, the chemical loss processes for pyruvic acid, isoprene, and MT (including photolysis and reactions with OH, O₃ and NO₃) are negligible. Initially disregarding the deposition of isoprene and MT, we derive lower limits of ($E_{\text{pyr}}/E_{\text{iso}}$) ~ 0.17 and ($E_{\text{pyr}}/E_{\text{MT}}$) ~ 4 (see Table 12). However, due to the presence of large concentrations of isoprene-consuming microbes in the soil of Biosphere 2, the isoprene loss rate

via deposition may be enhanced, which will decrease the effective emission ratio ($E_{\text{pyr}}/E_{\text{iso}}$). In addition, branch enclosure studies were performed on a *mangifera indica* (mango) tree within Biosphere 2, yielding mean fluxes (in nmol m⁻² s⁻¹) of 3.2 for isoprene, 0.09 for MT and 0.15 for pyruvic acid. Pyruvic acid emissions peaked during the day when temperature and photosynthetically active radiation (PAR) were highest and correlated very well with isoprene emissions and (to a certain extent) with MT emissions. Assuming that a mango tree is representative for the tropical vegetation, we derive emission ratio of ($E_{\text{pyr}}/E_{\text{iso}}$) ~ 0.05 and ($E_{\text{pyr}}/E_{\text{MT}}$) ~ 1.7 (see Table 12), which is consistent with our estimations for the IBairn campaign.

However, given that Talbot et al. (1990) observed great variability in pyruvic acid emission fluxes among five different tree species during measurements in the tropical Ducke Forest Reserve close to Manaus, Brazil, this agreement may, to some extent, be coincidental. Talbot et al. (1990) also reported a mean emission flux (derived from enclosure experiments) relative to isoprene of ($E_{\text{pyr}}/E_{\text{iso}}$) ~ 0.003 , which is about one order of magnitude smaller than in the study of Jardine et al. (2010b). In a further branch enclosure study by Jardine et al. (2010a) emissions from a creosotebush (*Larrea divaricata*), which is typically found in US drylands, were investigated. Average noontime branch emission rates (in $\mu\text{g C gdw}^{-1} \text{h}^{-1}$) of 7.5, 10.4 and 0.2 for isoprene, MT and pyruvic acid resulted in relative emission ratios of ($E_{\text{pyr}}/E_{\text{iso}}$) ~ 0.05 and ($E_{\text{pyr}}/E_{\text{MT}}$) ~ 0.07 for this mixed isoprene-MT-emitting species.

The comparison with the few datasets available in the literature indicates that the variability of the emission factors ($E_{\text{pyr}} / E_{\text{MT}}$) and ($E_{\text{pyr}} / E_{\text{iso}}$) among different plant species and different environments is large. In addition, a lack of pyruvic acid measurements over different seasons in the boreal forest means that we cannot exclude that the value we derive is biased by emissions (e.g., from ground-level, decaying plant-litter in September) that are peculiar to this season and environment. The emission rates ~~conclusions we derive raw from our following analysis~~ are therefore relevant for the autumnal boreal forest but require validation before being extended to other regions and seasons with confidence.

425 **3.2 Theoretical calculations on the fate of CH₃COH**

Singlet methylhydroxy carbene, CH₃COH, is best characterized as having an sp²-hybridized central carbon, bearing an in-plane lone pair in an sp² orbital and an empty p-orbital perpendicular to the CCO plane. The lone pairs of the hydroxy O-atom back-donate into the empty p-orbital, such that the most favourable geometry has the hydroxy-H-atom into the CCO plane. The orientation of the terminal OH group has a large impact on the energy, with 3 kcal mol⁻¹ energy difference between the *syn*- and *anti*-conformers. Due to the interaction between the hydroxy O-atom and the carbene functionality, internal rotation of the OH group has a very high barrier, 24 kcal mol⁻¹. Concomitantly, *syn/anti*-interconversion is very slow, with predicted rate coefficients at 300 K of less than 10⁻² s⁻¹. Under atmospheric conditions, thermalised *syn*- and *anti*-CH₃COH are thus best considered as separate species, with possibly distinct chemistry. No information is available on the relative yield of these conformers from pyruvic acid photolysis.

435 **3.2.1 Unimolecular reactions of CH₃COH**

Both *syn*- and *anti*-CH₃COH can isomerise to vinyl alcohol over high barriers ≥ 24 kcal mol⁻¹ (see Fig. 3). *Anti*-CH₃COH has an additional pathway for isomerisation to acetaldehyde, with a barrier of 23 kcal mol⁻¹. Due to these high barriers, the thermal rate of isomerisation is comparatively slow, with a 300 K rate coefficient of $\leq 4 \times 10^{-4}$ s⁻¹ (see Table 2). As already discussed by Schreiner et al. (2011), formation of CH₃CHO from *anti*-CH₃COH is most favourable at low temperatures owing to a thinner energy barrier and hence faster tunnelling. At temperatures above 260 K, we find that formation of CH₂=CHOH from *anti*-CH₃COH becomes dominant, with a ~3.5:1 ratio of CH₂=CHOH to CH₃CHO at room temperature.

Given the low predicted thermal rate coefficients, it seems unlikely that the experimentally observed acetaldehyde and vinyl alcohol in pyruvic acid photolysis are formed from isomerisation of *thermalized* CH₃COH. The energy distribution of energised, nascent carbenes would be rather broad as the available energy upon pyruvic acid photodissociation is distributed over all fragments and their relative motion, and the isomerisation yield would then be pressure-dependent. The CH₃CHO and CH₂=CH₂OH isomers formed would have enough energy to undergo keto-enol tautomerisation, but given the high barrier exceeding 55 kcal mol⁻¹ it is more probable they will instead be stabilized by collisional energy loss.

3.2.2 Reaction of CH₃COH with O₂

Under atmospheric conditions, the reaction with O₂ is potentially an important loss process for CH₃COH (Reed Harris et al., 2016; Reed Harris et al., 2017a; Eger et al., 2020). The potential energy surface is shown in Fig. 4. Contrary to radicals, which react with O₂ by (near-)barrierless radical recombination, the singlet CH₃COH carbene does not have an unpaired electron and the reaction proceeds mostly by association of its out-of-plane empty p-orbital with a lone electron pair in O₂, requiring orbital rearrangement to a triplet C[•]OO[•] moiety with a sp³-hybridized central carbon. This unfavourable process has high barriers, > 9 kcal mol⁻¹, and concomitantly low rate coefficients, $k(298\text{ K}) \sim 10^{-20}\text{ cm}^3\text{ molecule}^{-1}\text{ s}^{-1}$ (see Table 2). The rate coefficient is however highly uncertainly owing to an uncertainty (~1 to 2 kcal mol⁻¹) on the barrier height.

The decomposition of the CH₃C[•](OH)OO[•] triplet intermediate, forming CH₃C[•]=O + HO₂, is reminiscent of the chemistry of other α-OH alkyl radicals, and should occur rapidly owing to the sufficiently high energy content of the peroxy-alkyl diradical (Hermans et al., 2005, 2004; Dillon et al., 2012; Olivella et al., 2001; Dibble, 2002). The acyl radical product is expected to recombine rapidly with a second O₂ molecule, forming acylperoxy radicals, CH₃C(=O)OO[•]. Alternatively, the triplet CH₃C[•](OH)OO[•] intermediate can react with a second O₂ molecule by a barrierless recombination reaction (Fig. 4), forming the diperoxy singlet diradical CH₃C(OH)(OO[•])OO[•] which in turn can eliminate HO₂, similarly as other α-OH peroxy radicals, forming the acylperoxy radicals directly. This second O₂ addition is sufficiently exothermic to allow formation of peracetic acid with a singlet O₂ molecule, but this process has a rather large barrier of ~24 kcal mol⁻¹ and is expected to be a minor contributor, leaving CH₃C(O)O₂ + HO₂ as the likely dominant products of the overall reaction of CH₃COH with oxygen molecules.

3.2.3 Reactions of CH₃COH with carboxylic acids

Samanta et al. (2021) observed loss of CH₃COH via reaction with pyruvic acid, which may indicate that its fate in the atmosphere may also be (partially) controlled by similar reactions. To theoretically investigate the reaction of CH₃COH with carboxylic acids, we used formic acid in the calculations. Not only is formic acid an abundant organic acid in the atmospheric boundary layer, its reactivity is related to the properties of the -C(=O)OH moiety, and the results are transferable to other oxoacids, including pyruvic acid, which was present in high concentrations in most laboratory investigations.

As shown in Fig. 5, CH₃COH forms strong complexes with HC(O)OH, with 11 kcal mol⁻¹ stability. From this complex an addition process occurs that is best described as the transfer of the acidic H⁺ atom to the carbene lone pair on the CH₃COH central carbon, with simultaneous association of one of the negatively charged lone electron pair of the carbonyl oxygen to the carbene vacant p-orbital, forming a 1-hydroxyethylester. Due to the concerted association of the two carbene orbitals with suitable partners in the carboxylic moiety, this process has a very low barrier (≤ 1 kcal mol⁻¹). This mechanism is feasible due to the size of the -C(O)OH group, and the possibility of shifting the double bond to the other oxygen atom upon H-atom loss. For the anti-CH₃COH carbene, we also found that an in-plane approach of the carboxylic acid towards the COH moiety in methylhydroxy carbene can simultaneously transfer the acidic H-atom to the carbene carbon while the carbene hydroxy H-

480 atom is transferred to the carbonyl oxygen in the acid, reforming the HC(O)OH co-reactant. This catalysis reaction converts anti-CH₃COH to acetaldehyde, CH₃CHO, without an energy barrier. Both adduct formation and the catalysis reaction should proceed with rate coefficients near the collision limit.

Carboxylic acids can also catalyse keto-enol tautomerisation, possibly helping the isomerisation between CH₃CHO and CH₂=CH₂OH by reducing the effective barrier by over 50 kcal mol⁻¹ though the thermal reaction remains slow (see Table 2).
485 The only reaction of CH₃COH that has been investigated experimentally to date is that with pyruvic acid (Samanta et al., 2021), supplemented in this work by a theoretical exploration in the supporting information. Note that the large rate coefficient for CH₃COH with organic acids calculated here would imply that reaction of *thermalised* CH₃COH with pyruvic acid would overwhelm any other bimolecular CH₃COH reaction in their work and most of the experiments listed in Table S1.

3.2.4 Reactions of CH₃COH with H₂O

490 Based on the reactivity of small carbenes towards closed-shell molecules, Samanta et al. (2021) suggested that reaction with H₂O might be an important loss process of the CH₃COH carbene intermediate. We have characterized the insertion reaction of CH₃COH in the H₂O molecule, and found very high barriers, ≥ 11 kcal mol⁻¹, with very low rate coefficients $\sim 10^{-20}$ cm³ molecule⁻¹ s⁻¹ (see Fig. 5 and Table 2). The reaction is significantly slower than with carboxylic acid as the smaller H₂O molecule is unable to simultaneously reach both carbene orbitals in a favourable geometry. The reaction of H₂O with CH₃COH
495 is best described as a shift of an H⁺ atom to the carbene lone pair orbital, followed by migration of the water HO⁻ moiety to the vacant carbene orbital to form a bond with a lone electron pair. The reaction is further hindered by the back-donation of the CH₃COH oxygen atom into the vacant carbene orbital, partially filling the vacant carbene orbital and reducing the reactivity of the carbene functionality. We therefore propose that CH₃COH will be significantly less reactive towards closed shell species than the ²CH and ¹CH₂ carbenes which are known to exhibit very fast insertion and cyclo-addition reactions (Vereecken et al.,
500 1998; Goulay et al., 2009; Douglas et al., 2019; Jasper et al., 2007; Gannon et al., 2010).

3.2.5 Summary of theoretical calculations: The fate of *thermalised* CH₃COH in 1 bar of air

The theoretical analysis of the fate of CH₃COH carbene intermediates formed in PA photolysis indicates that the acetaldehyde formation observed in many experiments could be the result of a fast catalysis reaction of CH₃COH with pyruvic acid, which under typical experimental conditions exceeds competing reactions, such as with O₂, by several orders of magnitude. This
505 conclusion is consistent with the experimental observations of Reed Harris et al. (2017a) who report a reduction in the acetaldehyde yield when low pyruvic acid concentrations are used and an increase in the formation of acetic acid (which can be formed in the reaction of CH₃C(O)O₂ radicals with HO₂). In the atmospheric boundary layer atmosphere, where the concentrations of organic acids may lay between 10¹⁰ and 10¹¹ molecule cm⁻³ and that of O₂ is close to 5 × 10¹⁸ molecule cm⁻³ the reactions of CH₃COH with organic acids and O₂ are competitive, whereas reaction of CH₃COH with water is minor. Table
510 2 lists the predicted rate coefficients for these reactions.

3.3 Box-model results: Contribution of pyruvic acid to acetaldehyde and radical formation

3.2 Contribution of pyruvic acid to acetaldehyde and radical formation

To account for the large variability in photodissociation quantum yields and product yields reported in the literature (see above), we modelled two scenarios A and B:

515 **Scenario A:** In this scenario we used pyruvic acid cross sections, quantum yields and product yields according to the IUPAC recommendations (IUPAC, 2020) as listed in section 1.1.

Scenario B: Here we use the same absorption cross-sections as scenario A but build on the recent observations of (Samanta et al., 2021) and the theoretical work presented in section 3.2, which considers the formation and fate of an excited CH₃COH molecule (+ CO₂). In scenario B, we consider the effects of using photodissociation quantum yields of 0.2, 0.5 and 1 (scenarios
520 B_{0.2}, B_{0.5} and B₁, respectively).

In the box-model, photolysis at wavelengths < 340 nm was considered to generate CH₃CO + HOCO, whereas photolysis at wavelengths > 340 nm was assumed to form CO₂ + energy rich CH₃COH[#] which undergoes the reactions outlined in section 1.1. Assuming a quantum yield that is independent of wavelength results in 25 % of pyruvic acid photolysis at noon taking place at wavelengths < 340 nm and 75 % at wavelengths > 340 nm. In the model, we assume that this ratio does not change
525 (i.e. we neglect wavelength dependent variations in the relative actinic flux through the diel cycle). The values of 25% and 75 % listed above roughly correspond to the relative importance of peroxy radical formation (via R3, R4 and R5) at the shorter wavelengths compared to CH₃COH + CO₂ formation (R6) at the longer wavelengths. Some experimental data indicates that addition of O₂ can reduce the CH₃CHO yield in favour of formation of e.g. acetic acid. For this reason we use a rate coefficient for reaction of CH₃COH with O₂ that is competitive with the reaction between CH₃COH and organic acids. This is a factor
530 ~10 larger than the value obtained theoretically, but we consider this value still within the uncertainty (~1 to 2 kcal mol⁻¹ on the barrier height) of our current theoretical results as the peculiar wavefunction of CH₃COH may require even higher levels of theory to be described accurately.

In the box-model, in addition to reaction with O₂, the thermalised carbene also reacts with formic and acetic acids to form acetaldehyde:



with a rate coefficient of $5 \times 10^{-11} \text{ cm}^3 \text{ molecule}^{-1} \text{ s}^{-1}$.

We assumed that (at 1 bar) 70% of CH₃COH[#] was quenched to CH₃COH, 20% isomerised to CH₃CHO and 10% isomerised to CH₂=CHOH in order to reproduce the CH₃CHO-to-CH₂=CHOH ratio reported by Samanta et al. (2021). A summary
540 reaction scheme for the photodissociation of pyruvic acid and the fate of the initial products is given in the SI.

3.3.1 CH₃CHO formation

The modelled formation of CH₃CHO from pyruvic acid photolysis through the diel cycle when considering scenario A is displayed as a stacked plot of contributing reactions in Fig. 6. Immediately apparent from this figure is the dominance of pyruvic acid photolysis compared to all other processes. Under scenario A, even with the low quantum yield ($\phi = 0.2$) recommended by IUPAC, pyruvic acid photolysis contributes > 80 % to the overall CH₃CHO production term, with a maximum of ~15% (at noon) arising from reactions of the ethylperoxy radical, formed in the reaction of OH with ethane (7.5%) and butane (3.75 %) and in the photolysis of CH₃C(O)C₂H₅ (3.75 %).

Under scenario B, pyruvic acid photolysis still dominates the formation of CH₃CHO, with a noon-time contribution of 91%, 86 % and 71% when quantum yields of 1, 0.5 and 0.2 are considered. Of the pyruvic acid contribution, 45% of the CH₃CHO arises via isomerisation of the initially formed, energised carbene (blue), while the remaining 55 % results from reactions of the thermalised carbene with formic (orange) and acetic (green) acids, the concentrations of which were constrained by observations. The modelled, noon-time mixing ratio of CH₃CHO varies from 400 pptv (scenario B₁) to 160 pptv (scenario B_{0.2}) when pyruvic acid photolysis is included and is reduced to ~100 pptv when the quantum yield is set to zero. Unfortunately, reliable measurements of the CH₃CHO mixing ratios with which to compare the model simulations were not available for the IBairn campaign as the in-situ PTRMS data set (*m/z* 45) varied from -400 to + 400 pptv over the diel cycle. The modelled, maximum mixing ratio of CH₃CHO increase from ~100 pptv when pyruvic acid photolysis is neglected to > 400 pptv under scenario B₁. (see Fig. S

3.3.2 CH₃C(O)O₂ formation

The CH₃C(O)O₂ radical is formed in a termolecular reaction between the CH₃CO radical and O₂. Figure 7 displays the main photochemical reactions that lead to the formation of CH₃CO in our model. The spikes in the simulated production rates are connected to spikes in the diel average NO mixing ratio at the site. In analysing the data we therefore consider not only the contributions at noon (when, coincidentally NO mixing ratios were large) but also at 10:30 when NO mixing ratios were comparably low.

Under scenario A, where $\phi = 0.2$ and the yield of the CH₃CO radical is 0.35, the contribution of pyruvic acid photolysis to the overall production rate at 12:00 and 10:30 are about 23 % and 16 %, respectively, which are roughly equally divided into a direct contribution (J43018) and an indirect contribution (G42008a) arising via enhanced CH₃CHO levels. The main contributors to the formation of CH₃CO are reactions initiated by the degradation of isoprene and monoterpenes (in the legend to Fig. 5: BIACETO2, C511O₂, C716O₂, CO23C4CHO, CO235C6CHO) which involve reactions of peroxy radicals with NO. Under scenario B₁, the photolysis of pyruvic acid become significantly more important, contributing a total of 63% of the total production rate for CH₃CO at 10:30 and 42% at 12:00. When considering scenarios B_{0.5} and B_{0.2} the contributions of pyruvic acid photolysis are reduced to 46 % (29%) and 29% (17%), respectively, where the numbers in parentheses are for the “high NO_x” situation. Generally, the reaction of the thermalised carbene with O₂ (G42099), the direct photolysis at wavelengths <

340 nm (J43018) and the indirect enhancement in CH₃CO formation via the enhanced levels of CH₃CHO (G42008a) contribute roughly equally to the formation of CH₃CO resulting from pyruvic acid photolysis. The modelled mixing ratio of the CH₃C(O)O₂ radical at noon increases by a factor ~1.5 when comparing scenario B1 with the quantum yields for pyruvic acid photodissociation set to zero.

3.3.3 HO₂ formation

In Fig. 8 we plot the 9 most important model pathways to HO₂ production through the diel cycle. The dominant modelled production terms for HO₂ involve HCHO (photolysis HCHO and reaction with OH, G4108, J41001b), the reaction of methoxy radicals (G4118, whereby CH₃O is generated mainly in the reaction of CH₃O₂ radicals with NO) and the reaction of OH with CO. The direct contribution of pyruvic acid photolysis to HO₂ formation (via its photolysis (J43018) and through the reaction of CH₃COH with O₂ (G42099)) is ~ 10% under scenario B₁ under low NO_x conditions (i.e. at 10:30). Under all other scenarios it is lower with values (in percent) of <1 (scenario A at both 10:30 and 2:00), ~6 (scenario B1 at 12:00), ~5 and ~3.5 (scenario B_{0.5} at 10:30 and 12:00, respectively) and ~1.5 and <1 (scenario B_{0.2} at 10:30 and 12:00, respectively). However, although the direct impact of pyruvic acid photolysis is weak, it has a significant indirect effect via the enhanced formation of CH₃C(O)O₂ radicals (directly via R3 + R4 and R10 and indirectly via CH₃CHO formation) which, in the presence of O₂ reacts with NO to form CH₃O₂. Enhanced production rates of CH₃O₂ result in enhanced production rates of CH₃O and HCHO and thus HO₂.



The model simulations have shown that the photolysis of pyruvic acid at the levels observed during the IBAIRN campaign have a potentially significant effect on both CH₃CHO mixing ratios and production rates of HO₂ and CH₃C(O)O₂ radicals, the latter being especially enhanced under low-NO_x conditions. The enhanced production rates and concentrations of CH₃C(O)O₂ and HO₂ also results in significant increases in the modelled mixing ratios of several trace gases that are formed from these radicals. When comparing scenario B₁ to the case when the pyruvic acid photodissociation quantum yield (ϕ) is set to zero results in an increase by factors of 2.2, 2.0 and 1.6 for CH₃C(O)OOH, CH₃OOH and H₂O₂ and HCHO, respectively (see Fig S5). HCHO mixing ratios are enhanced by a factor 1.2. Vinyl alcohol mixing ratios of up to 40 pptv were generated in scenario B1. Clearly, the photolysis of pyruvic acid can potentially impact strongly on the concentrations of e.g. C1 and C2 carbonyl compounds and peroxides in the boreal environment.

~~To quantify the impact of pyruvic acid photolysis during IBAIRN, we identified the relative contributions of the processes forming OH, HO₂, CH₃C(O)O₂, CH₃CHO, HCHO and CH₃OOH from our model runs, and compared scenario A (the reference~~

605 run with no impact from pyruvic acid) with scenarios B and C. The campaign-averaged production rates are summarised in Table 3.

Figure 3 illustrates the relative importance of the various pathways to OH formation and the resulting OH concentrations for the three different scenarios. On average, the main source of OH radicals was the direct formation from O₃ photolysis (39 % in scenario B), followed by the reaction of HO₂ with NO (30 %) and O₂ + MT (25 %). The inclusion of pyruvic acid photolysis in the model increased the relative importance of the HO₂ + NO reaction by 1 % (scenario B) or 6 % (scenario C) due to increased HO₂ production. The overall OH production rate ($13.1 \times 10^5 \text{ molec cm}^{-3} \text{ s}^{-1}$ in scenario A, see Table 3) increases by 2 % in scenario B or 13 % when considering scenario C.

For HO₂ (Fig. 4) the three major sources during IBAIRN were the reactions OH + CO (39 %), RO₂ + NO (36 %), and CH₃O₂ + NO (19 %). In scenario B, pyruvic acid accounts for just 2 % of the total HO₂ production (via R2 and R5, see Fig. 1) whereas in scenario C this increases to 14 % (via R1 and R7). The overall HO₂ production rate ($5.8 \times 10^5 \text{ molec cm}^{-3} \text{ s}^{-1}$ in scenario A, see Table 3) increases by just 2 % in scenario B but by as much as 36 % in scenario C. Clearly, the combination of a high quantum yield of pyruvic acid photolysis and direct formation of radicals can have a significant impact on the HO_x budget. As the photolysis of pyruvic acid occurs at wavelengths that are red-shifted compared to O₃ photolysis, the model predicts that the onset of photochemical radical formation in scenario C is about 1 hour earlier than without pyruvic acid photolysis.

620 Figure 5 summaries the results for CH₃C(O)O₂. The most important channel for CH₃C(O)O₂ production in Scenario A was by far the decomposition of PAN (95 %), followed by OH + CH₃CHO (5 %). When comparing scenario B with A, the overall CH₃C(O)O₂ production rate is slightly increased due to the presence of pyruvic acid, with a contribution of 8 % directly arising from its photolysis (CH₃C(O)C(O)OH + *hν*). In scenario C, the contribution from the photolysis of pyruvic acid increases to 52 % and the overall CH₃C(O)O₂ production rate almost doubles. This would make pyruvic acid an important source of CH₃C(O)O₂ during the IBAIRN campaign. In scenario C we also see a clear shift in the onset of radical generation to earlier in the morning when actinic flux is dominated by wavelengths that are too long to initiate ozone photolysis but are absorbed by pyruvic acid.

In the absence of pyruvic acid photolysis (scenario A), the production of acetaldehyde is dominated by the degradation of alkanes (n-butane, ethane, and propane). When including formation of CH₃CHO via pyruvic acid photolysis in scenario B (Fig. 6), the contribution of the alkanes drastically decreases, and pyruvic acid becomes the dominant source of acetaldehyde (79 %) in this environment. The fractional contribution remains high (53 %) in scenario C even though CH₃CHO is formed only at low yield (5 %) in this case. The pyruvic acid mixing ratios observed during IBAIRN would result in mean simulated acetaldehyde mixing ratios of ~115 pptv (Fig. 6d), which is reasonable for this site as shown in the HUMPPA dataset (Sect. 3.3).

635 The three main sources of the CH₃O₂ radical in air are the reactions CH₄ + OH, CH₃C(O)O₂ + HO₂ and CH₃C(O)O₂ + NO, all preceding via formation of the CH₃ radical, in the last two cases a result of decomposition of the unstable intermediate CH₃CO₂. The CH₃O₂ radical is a source of both the most abundant aldehyde (HCHO) and methyl hydroperoxide (CH₃OOH) in the troposphere, the former preferentially formed at high NO_x levels, the latter under low NO_x conditions. As shown in Fig. 7,

pyruvic acid photolysis increases the fraction of CH_3O_2 formed from $\text{CH}_3\text{C}(\text{O})\text{O}_2$ to 5 % (scenario B) and 18 % (scenario C), with methane oxidation still accounting for most of the total production rate. In scenario C, the summed production rates of HCHO and CH_3OOH are increased by 42 % each (Table 3).

3.3 Summer campaign (HUMPPA): Contribution of pyruvic acid to acetaldehyde and $\text{CH}_3\text{C}(\text{O})\text{O}_2$ formation

As pyruvic acid was not measured during HUMPPA, we use the calculated mean emission rate of pyruvic acid relative to MT during IBAIRN (derived from Eq. 2, see Table 1) as an input parameter for the HUMPPA simulation to estimate the pyruvic acid mixing ratios (in steady state) shown in Fig. 8.

Compared with IBAIRN, where $[\text{pyr}] / [\text{MT}] \sim 0.3$ on average, for HUMPPA the mean concentration ratio is ~ 1.6 , which is mainly a consequence of the higher temperatures and larger MXL heights during the summertime HUMPPA campaign (especially at night) which result in lower pyruvic acid deposition rates. In addition, it is also influenced by the higher OH and O_3 levels in summer (HUMPPA) which contribute to MT losses. The highest pyruvic acid mixing ratios are modelled for the night time (lowest h_{MXL}) and in periods impacted by biomass burning from Russia, which is indicated by elevated CO and HCN levels (periods highlighted in light blue). Coincidentally, the biomass burning periods were accompanied by high temperatures and high MT levels also. When excluding the biomass burning periods from the analysis, simulated pyruvic acid mixing ratios occasionally reach values up to ~ 2 ppbv with a mean campaign value of ~ 0.5 ppbv.

Similar to the autumn campaign IBAIRN we can now quantify the contribution of pyruvic acid photolysis to the formation of acetaldehyde, peroxy radicals and PAA. Therefore, we compare Scenarios A with B and C (as for the IBAIRN simulation in Sect. 3.2), in this case focussing on the $\text{CH}_3\text{C}(\text{O})\text{O}_2$ radical and on acetaldehyde as both are precursors to $\text{CH}_3\text{C}(\text{O})\text{OOH}$, which was measured during HUMPPA.

In the absence of pyruvic acid photolysis (Scenario A), the production of acetaldehyde is dominated by n-butane, ethane, and propane. However, these globally important CH_3CHO precursors are not sufficient to explain the acetaldehyde concentrations that were observed (Fig. 8). Another potential source is the direct biogenic emission from vegetation (see e.g. Rissanen et al. (2020), making up ~ 15 % of the total CH_3CHO source (Millet et al., 2010). However, on a global scale (and also in Finland) these emissions are a factor of ~ 5 smaller than the photochemical production term and have thus been neglected in the simulation. By enabling formation of CH_3CHO via pyruvic acid photolysis in Scenario B (see Fig. 9), the contribution of the alkanes reduces to 6 % and pyruvic acid becomes the dominant source of acetaldehyde (94 % in scenario B, 76 % in scenario C) during HUMPPA. Removing periods impacted by biomass burning plumes does not significantly change the overall conclusions (pyruvic acid contribution decreases by ~ 2 %). When comparing the time series of measured acetaldehyde mixing ratios with the model output (Fig. 8), we note that scenario B more closely reproduces the observations than scenario A which greatly underpredicts the observed CH_3CHO for much of the campaign. We conclude that pyruvic acid photolysis represents a potentially important contribution to acetaldehyde mixing ratios in the boreal forest and possibly also on a global scale (above forested regions).

The major source of acetylperoxy radical in Scenario A is the decomposition of PAN (93 %), with a minor contribution from the oxidation of acetaldehyde (7 %) (see Fig. 10). In Scenario B, the direct impact of pyruvic acid photolysis on $\text{CH}_3\text{C}(\text{O})\text{O}_2$ is 3 %, whereas the indirect impact from the formation of acetaldehyde and its subsequent oxidation via $\text{CH}_3\text{CHO} + \text{OH}$ is negligible. In contrast, in Scenario C, the direct contribution from the photolysis of pyruvic acid is 19 %, making pyruvic acid an important contributor to acetylperoxy radical generation in this environment and underlining the importance of dicarbonyls, as suggested by Crowley et al. (2018). However, the pyruvic acid mixing ratios alone (without other dicarbonyls) cannot explain the observed large PAA mixing ratios during HUMPPA (Crowley et al., 2018), especially during the biomass burning episodes.

4 Conclusions

We have combined measurements of pyruvic acid in an autumn campaign in the boreal forest (IBAIRN) with theoretical calculations designed to characterise the fate of the methylhydroxy carbene radical (CH_3COH), which is the major product of its photodissociation with a box modelling study to study the impact of its photolysis on the rates of production of acetaldehyde (CH_3CHO) and the peroxy radicals $\text{CH}_3\text{C}(\text{O})\text{O}_2$ and HO_2 . The theoretical study revealed unexpected features of CH_3COH chemistry, including slow reactions of thermalised carbene with H_2O but an efficient acid-catalysed conversion to CH_3CHO in the presence of organic acids such as $\text{HC}(\text{O})\text{OH}$. The reaction of CH_3COH with O_2 is slow, but will likely contribute to its fate (and thus the formation of $\text{CH}_3\text{C}(\text{O})\text{O}_2$ and HO_2) in the lower atmosphere where O_2 concentrations are high.

In our box-model, the photolysis of pyruvic acid was parameterised as presently recommended by IUPAC (whereby the main products are CH_3CHO and CO_2) and also using a more detailed mechanism in which the formation and fate of CH_3COH was considered and in which the quantum yield was also varied. In all scenarios, we find that the photolysis of pyruvic acid was the dominant source of CH_3CHO during IBAIRN and that its instantaneous contribution to the daytime formation of $\text{CH}_3\text{C}(\text{O})\text{O}_2$ varied between 16 and 63 %, dependent on the assumed scenario and also on the NO concentration. Pyruvic acid photodissociations results in a significant increase in the mixing ratios of several carbonyl compounds and peroxides in the boreal environment.

Using pyruvic acid cross sections and quantum yields ($\phi = 0.2$) according to the IUPAC recommendations (scenario B in which the dominant photolysis products are $\text{CH}_3\text{CHO} + \text{CO}_2$), we identified pyruvic acid as an important source of acetaldehyde (CH_3CHO) in both autumn (IBAIRN) and summer (HUMPPA) with a contribution of 79 % respectively 94 % to the overall production rate. Pyruvic acid may thus have contributed to the source of elevated mixing ratios of acetaldehyde observed during HUMPPA which could not be explained by the degradation of alkanes. Our results might also help to explain the discrepancies between modelled and observed CH_3CHO mixing ratios in remote, forested regions where emissions of pyruvic acid may be significant. In contrast, under scenario B, the effect on OH , HO_2 , $\text{CH}_3\text{C}(\text{O})\text{O}_2$ and HCHO formation rates during both campaigns is minor ($< 10\%$).

This picture changes drastically under scenario C, whereby the quantum yield is a factor of ~4 larger and formation of HO₂ and CH₃C(O)O₂ is preferred over CH₃CHO. In both campaigns pyruvic acid now increases the overall HO₂ production by ~20–35 % and the overall HCHO production by ~25–40 %. In scenario C, pyruvic acid photolysis is comparable to PAN decomposition as source of CH₃C(O)O₂ during IBAIRN, also shifting the onset of radical production to earlier in the morning. The presence of pyruvic acid can partly explain the elevated PAA mixing ratios observed in HUMPPA, though other oxygenates might play a role as well, especially during biomass burning events (Crowley et al., 2018).

The results of our modelling study are strongly dependent on the chosen quantum yields and photodissociation mechanism. To reduce the uncertainty in the role of pyruvic acid photolysis, there is an urgent need for further experimental and theoretical work on the photochemistry of pyruvic acid and on the fate of methylhydroxy carbene under atmospheric conditions. In addition, further measurements of pyruvic acid mixing ratios and of its deposition velocity in different environments are required to better constrain its abundance, lifetime and thus the impact of its photolysis. Enclosure studies would be helpful to investigate the dependence of pyruvic acid emission rates on different plant types and environmental conditions. In general, our results are strongly dependent on the chosen quantum yields and deposition velocities. To minimise the uncertainty in our calculations, there is an urgent need for further experimental work on the photochemistry of pyruvic acid. In addition, measurements of the deposition velocity of pyruvic acid in different environments are required to better constrain its lifetime and thus the impact of photolysis. Further, more enclosure studies will be necessary to investigate the dependence of pyruvic acid emission rates on different plant types and environmental conditions.

Data availability

The Max Planck Institute data used for the IBAIRN analysis and the reaction scheme used in the box-model are archived with Zenodo at <https://doi.org/10.5281/zenodo.3254828> (Crowley and Fischer, 2019). HUMPPA-COPEC-2010 data can be obtained on request (via John N. Crowley) from the owners.

Author contributions

PGE was responsible for the pyruvic acid measurement during IBAIRN. PE and JC, and with contributions from JNC and JL, ran the box model, analysed the model results for the IBAIRN and HUMPPA campaigns and wrote the manuscript. LV made the theoretical calculation on the fate of methylhydroxy carbene, RS and AP did the box-modelling, NS was responsible for the CRDS measurements of NO₂ and PANs during IBAIRN. JS was responsible for the O₃ and J-value measurements during IBAIRN. HF was responsible for the NO and CO measurements during IBAIRN and HUMPPA. EK and JW were responsible for the monoterpene measurements during IBAIRN. VV was responsible for the mixing layer height measurements during IBAIRN. TP was responsible for the SMEAR II observations and infrastructure. All authors contributed to the paper.

Competing interests

The authors declare that they have no conflict of interest.

Acknowledgements

We thank the technical staff of SMEAR II station for the excellent support during IB AIRN ~~and HUMPPA-COPEC~~.

735 Financial support

We are grateful to ENVRIplus for partial financial support of the IB AIRN campaign.

References

- 740 Aalto, J., Porcar-Castell, A., Atherton, J., Kolari, P., Pohja, T., Hari, P., Nikinmaa, E., Petaja, T., and Back, J.: Onset of photosynthesis in spring speeds up monoterpene synthesis and leads to emission bursts, *Plant Cell Environ.*, 38, 2299-2312, doi:10.1111/pce.12550, 2015.
- Andreae, M. O., Talbot, R. W., and Li, S. M.: Atmospheric measurements of pyruvic and formic acid, *J. Geophys. Res. - Atmos.*, 92, 6635-6641, doi:10.1029/JD092iD06p06635, 1987.
- 745 Berges, M. G. M., and Warneck, P.: Product quantum yields for the 350 nm photodecomposition of pyruvic-acid in air, *Berichte Der Bunsen-Gesellschaft-Physical Chemistry Chemical Physics*, 96, 413-416, doi:10.1002/bbpc.19920960334, 1992.
- Burkholder, J. B., Sander, S. P., Abbatt, J., Barker, J. R., Huie, R. E., Kolb, C. E., Kurylo, M. J., Orkin, V. L., Wilmouth, D. M., and Wine, P. H.: Chemical Kinetics and Photochemical Data for Use in Atmospheric Studies, Evaluation No. 18," JPL Publication 15-10, Jet Propulsion Laboratory, Pasadena, <http://jpldataeval.jpl.nasa.gov>, 2015.
- 750 Calvert, J. G., Mellouki, A., Pilling, M. J., and Wallington, T. J.: *The Mechanisms of Atmospheric Oxidation of the Oxygenates*, Oxford Univ. Press, New York, 2011.
- Chang, X.-P., Fang, Q., and Cui, G.: Mechanistic photodecarboxylation of pyruvic acid: Excited-state proton transfer and three-state intersection, *The Journal of Chemical Physics*, 141, 154311, doi:10.1063/1.4898085, 2014.
- 755 Crowley, J. N., Pouvesle, N., Phillips, G. J., Axinte, R., Fischer, H., Petäjä, T., Nölscher, A., Williams, J., Hens, K., Harder, H., Martinez-Harder, M., Novelli, A., Kubistin, D., Bohn, B., and Lelieveld, J.: Insights into HO_x and RO_x chemistry in the boreal forest via measurement of peroxyacetic acid, peroxyacetic nitric anhydride (PAN) and hydrogen peroxide, *Atmos. Chem. Phys.*, 18, 13457-13479, doi:10.5194/acp-18-13457-2018, 2018.
- 760 Dee, D. P., Uppala, S. M., Simmons, A. J., Berrisford, P., Poli, P., Kobayashi, S., Andrae, U., Balmaseda, M. A., Balsamo, G., Bauer, P., Bechtold, P., Beljaars, A. C. M., van de Berg, L., Bidlot, J., Bormann, N., Delsol, C., Dragani, R., Fuentes, M., Geer, A. J., Haimberger, L., Healy, S. B., Hersbach, H., Hólm, E. V., Isaksen, L., Kållberg, P., Köhler, M., Matricardi, M., McNally, A. P., Monge-Sanz, B. M., Morcrette, J.-J., Park, B.-K., Peubey, C., de Rosnay, P., Tavalato, C., Thépaut, J.-N.,

- and Vitart, F.: The ERA-Interim reanalysis: configuration and performance of the data assimilation system, *Quarterly Journal of the Royal Meteorological Society*, 137, 553-597, doi:10.1002/qj.828, 2011.
- 765 Eger, P. G., Schuladen, J., Sobanski, N., Fischer, H., Karu, E., Williams, J., Riva, M., Zha, Q., Ehn, M., Quéléver, L. L. J., Schallhart, S., Lelieveld, J., and Crowley, J. N.: Pyruvic acid in the boreal forest: gas-phase mixing ratios and impact on radical chemistry, *Atmos. Chem. Phys.*, 20, 3697-3711, doi:10.5194/acp-20-3697-2020, 2020.
- Eugene, A. J., Pillar, E. A., Colussi, A. J., and Guzman, M. I.: Enhanced Acidity of Acetic and Pyruvic Acids on the Surface of Water, *Langmuir*, 34, 9307-9313, doi:10.1021/acs.langmuir.8b01606, 2018.
- 770 Fischer, H., Axinte, R., Bozem, H., Crowley, J. N., Ernest, C., Gilge, S., Hafermann, S., Harder, H., Hens, K., Janssen, R. H. H., Königstedt, R., Kubistin, D., Mallik, C., Martinez, M., Novelli, A., Parchatka, U., Plass-Dülmer, C., Pozzer, A., Regelin, E., Reiffs, A., Schmidt, T., Schuladen, J., and Lelieveld, J.: Diurnal variability, photochemical production and loss processes of hydrogen peroxide in the boundary layer over Europe, *Atmos. Chem. Phys.*, 19, 11953-11968, doi:10.5194/acp-19-11953-2019, 2019.
- 775 Fischer, L., Breitenlechner, M., Canaval, E., Scholz, W., Striednig, M., Graus, M., Karl, T. G., Petäjä, T., Kulmala, M., and Hansel, A.: First Eddy Covariance Flux Measurements of Semi Volatile Organic Compounds with the PTR3-TOF-MS, *Atmos. Meas. Tech. Discuss.*, 2021, 1-28, doi:10.5194/amt-2021-117, 2021.
- Gaona-Colman, E., Blanco, M. B., Barnes, I., Wiesen, P., and Teruel, M. A.: OH- and O-3-initiated atmospheric degradation of camphene: temperature dependent rate coefficients, product yields and mechanisms, *Rsc Advances*, 7, 2733-2744, doi:10.1039/c6ra26656h, 2017.
- 780 Grosjean, D.: Atmospheric reactions of pyruvic acid, *Atmospheric Environment (1967)*, 17, 2379-2382, doi:10.1016/0004-6981(83)90242-1, 1983.
- Grosjean, D.: Atmospheric reactions of ortho cresol: gas phase and aerosol products, *Atmospheric Environment (1967)*, 18, 1641-1652, doi:10.1016/0004-6981(84)90386-X, 1984.
- Grosjean, D., Williams, E. L., and Grosjean, E.: Atmospheric chemistry of isoprene and of its carbonyl products, *Env. Sci. Tech.*, 27, 830-840, doi:10.1021/es00042a004, 1993.
- 785 Guenther, A. B., Zimmerman, P. R., Harley, P. C., Monson, R. K., and Fall, R.: Isoprene and monoterpene emission rate variability - model evaluations and sensitivity analyses, *J. Geophys. Res. -Atmos.*, 98, 12609-12617, doi:10.1029/93jd00527, 1993.
- Hakola, H., Hellén, H., and Laurila, T.: Ten years of light hydrocarbons (C₂–C₆) concentration measurements in background air in Finland, *Atmos. Env.*, 40, 3621-3630, doi:10.1016/j.atmosenv.2005.08.019, 2006.
- 790 Hallquist, M., Wenger, J. C., Baltensperger, U., Rudich, Y., Simpson, D., Claeys, M., Dommen, J., Donahue, N., George, C., and Goldstein, A.: The formation, properties and impact of secondary organic aerosol: current and emerging issues, *Atmos. Chem. Phys.*, 9, 5155-5236, doi:10.5194/acp-9-5155-2009, 2009.
- Hari, P., and Kulmala, M.: Station for Measuring Ecosystem–Atmosphere Relations (SMEAR II), *Boreal Env. Res.*, 10, 315–322, doi:10.1007/978-94-007-5603-8_9, 2005.
- 795 Helas, G., Bingemer, H., and Andreae, M. O.: Organic acids over equatorial Africa: Results from DECAFE 88, *Journal of Geophysical Research: Atmospheres*, 97, 6187-6193, doi:10.1029/91jd01438, 1992.

- Hellén, H., Kouznetsov, R., Anttila, P., and Hakola, H.: Increasing influence of easterly air masses on NMHC concentrations at the Pallas-Sodankylä GAW station, 2015.
- 800 Hellén, H., Praplan, A. P., Tykkä, T., Ylivinkka, I., Vakkari, V., Bäck, J., Petäjä, T., Kulmala, M., and Hakola, H.: Long-term measurements of volatile organic compounds highlight the importance of sesquiterpenes for the atmospheric chemistry of a boreal forest, *Atmos. Chem. Phys.*, 18, 13839-13863, doi:10.5194/acp-18-13839-2018, 2018.
- Task Group on Atmospheric Chemical Kinetic Data Evaluation, (Ammann, M., Cox, R.A., Crowley, J.N., Herrmann, H., Jenkin, M.E., McNeill, V.F., Mellouki, A., Rossi, M. J., Troe, J. and Wallington, T. J.): <http://iupac.pole-ether.fr/index.html>, 2020.
- 805 Task Group on Atmospheric Chemical Kinetic Data Evaluation, (Ammann, M., Cox, R.A., Crowley, J.N., Herrmann, H., Jenkin, M.E., McNeill, V.F., Mellouki, A., Rossi, M. J., Troe, J. and Wallington, T. J.): <http://iupac.pole-ether.fr/index.html>, 2021.
- Jacob, D. J., and Wofsy, S. C.: Photochemistry of biogenic emissions over the Amazon forest, *J. Geophys. Res. -Atmos.*, 93, 1477-1486, doi:10.1029/JD093iD02p01477, 1988.
- 810 Jardine, K., Abrell, L., Kurc, S. A., Huxman, T., Ortega, J., and Guenther, A.: Volatile organic compound emissions from *Larrea tridentata* (creosotebush), *Atmos. Chem. Phys.*, 10, 12191-12206, doi:10.5194/acp-10-12191-2010, 2010a.
- Jardine, K. J., Sommer, E. D., Saleska, S. R., Huxman, T. E., Harley, P. C., and Abrell, L.: Gas Phase Measurements of Pyruvic Acid and Its Volatile Metabolites, *Env. Sci. Tech.*, 44, 2454-2460, doi:10.1021/es903544p, 2010b.
- 815 Kanakidou, M., Seinfeld, J., Pandis, S., Barnes, I., Dentener, F., Facchini, M., Dingenen, R. V., Ervens, B., Nenes, A., and Nielsen, C.: Organic aerosol and global climate modelling: a review, *Atmos. Chem. Phys.*, 5, 1053-1123, doi:10.5194/acp-5-1053-2005, 2005.
- Liebmann, J., Karu, E., Sobanski, N., Schuladen, J., Ehn, M., Schallhart, S., Quéléver, L., Hellen, H., Hakola, H., Hoffmann, T., Williams, J., Fischer, H., Lelieveld, J., and Crowley, J. N.: Direct measurement of NO₃ radical reactivity in a boreal forest, *Atmos. Chem. Phys.*, 2018, 3799-3815, doi:10.5194/acp-18-3799-2018, 2018a.
- 820 Liebmann, J., Sobanski, N., Schuladen, J., Karu, E., Hellén, H., Hakola, H., Zha, Q., Ehn, M., Riva, M., Heikkinen, L., Williams, J., Fische, H., Lelieveld, J., and Crowley, J. N.: Alkyl nitrates in the boreal forest: formation via the NO₃-, OH- and O₃-induced oxidation of biogenic volatile organic compounds and ambient lifetimes, *Atmos. Chem. Phys.*, 19, 10391-10403, doi:10.5194/acp-19-10391-2019, 2019.
- 825 Liebmann, J. M., Muller, J. B. A., Kubistin, D., Claude, A., Holla, R., Plass-Dülmer, C., Lelieveld, J., and Crowley, J. N.: Direct measurements of NO₃ reactivity in and above the boundary layer of a mountaintop site: identification of reactive trace gases and comparison with OH reactivity, *Atmos. Chem. Phys.*, 18, 12045-12059, doi:10.5194/acp-18-12045-2018, 2018b.
- Mellouki, A., and Mu, Y.: On the atmospheric degradation of pyruvic acid in the gas phase, *Journal of Photochemistry and Photobiology A: Chemistry*, 157, 295-300, doi:10.1016/S1010-6030(03)00070-4, 2003.
- 830 Millet, D. B., Guenther, A., Siegel, D. A., Nelson, N. B., Singh, H. B., de Gouw, J. A., Warneke, C., Williams, J., Eerdekens, G., and Sinha, V.: Global atmospheric budget of acetaldehyde: 3-D model analysis and constraints from in-situ and satellite observations, *Atmos. Chem. Phys.*, 10, 3405-3425, doi:10.5194/acp-10-3405-2010, 2010.

- Paulot, F., Crounse, J. D., Kjaergaard, H. G., Kroll, J. H., Seinfeld, J. H., and Wennberg, P. O.: Isoprene photooxidation: new insights into the production of acids and organic nitrates, *Atmos. Chem. Phys.*, 9, 1479-1501, doi:10.5194/acp-9-1479-2009, 2009.
- 835 Perring, A. E., Pusede, S. E., and Cohen, R. C.: An observational perspective on the atmospheric impacts of alkyl and multifunctional nitrates on ozone and secondary organic aerosol, *Chem. Rev.*, 113, 5848-5870, doi:10.1021/cr300520x, 2013.
- Petäjä, T., Mauldin, I. R. L., Kosciuch, E., McGrath, J., Nieminen, T., Paasonen, P., Boy, M., Adamov, A., Kotiaho, T., and Kulmala, M.: Sulfuric acid and OH concentrations in a boreal forest site, *Atmos. Chem. Phys.*, 9, 7435-7448, doi:10.5194/acp-9-7435-2009, 2009.
- 840 Praplan, A. P., Hegyi-Gaeggeler, K., Barmet, P., Pfaffenberger, L., Dommen, J., and Baltensperger, U.: Online measurements of water-soluble organic acids in the gas and aerosol phase from the photooxidation of 1, 3, 5-trimethylbenzene, *Atmos. Chem. Phys.*, 14, 8665-8677, doi:10.5194/acp-14-8665-2014, 2014.
- Raber, W. H., and Moortgat, G. K.: Photooxidation of selected carbonyl compounds in air: methyl ethyl ketone, methyl vinyl ketone, methacrolein and methylglyoxal, *Progress and problems in atmospheric chemistry*, edited by: Barker, JR, World Scientific Publishing, Singapore, 318-373, 1995.
- 845 Reed Harris, A. E., Doussin, J. F., Carpenter, B. K., and Vaida, V.: Gas-Phase Photolysis of Pyruvic Acid: The Effect of Pressure on Reaction Rates and Products, *J. Phys. Chem. A*, 120, 10123-10133, doi:10.1021/acs.jpca.6b09058, 2016.
- Reed Harris, A. E., Cazaunau, M., Gratien, A., Pangu, E., Doussin, J.-F., and Vaida, V.: Atmospheric Simulation Chamber Studies of the Gas-Phase Photolysis of Pyruvic Acid, *J. Phys. Chem. A*, 121, 8348-8358, doi:10.1021/acs.jpca.7b05139, 2017a.
- 850 Reed Harris, A. E., Cazaunau, M., Gratien, A., Pangu, E., Doussin, J. F., and Vaida, V.: Atmospheric Simulation Chamber Studies of the Gas-Phase Photolysis of Pyruvic Acid, *J. Phys. Chem. A*, 121, 8348-8358, doi:10.1021/acs.jpca.7b05139, 2017b.
- 855 Rinne, J., Hakola, H., Laurila, T., and Rannik, Ü.: Canopy scale monoterpene emissions of *Pinus sylvestris* dominated forests, *Atmos. Env.*, 34, 1099-1107, doi:[https://doi.org/10.1016/S1352-2310\(99\)00335-0](https://doi.org/10.1016/S1352-2310(99)00335-0), 2000.
- Roberts, J. M., Flocke, F., Chen, G., de Gouw, J., Holloway, J. S., Hübler, G., Neuman, J. A., Nicks Jr., D. K., Nowak, J. B., Parrish, D. D., Ryerson, T. B., Sueper, D. T., Warneke, C., and Fehsenfeld, F. C.: Measurement of peroxy-carboxylic nitric anhydrides (PANs) during the ITCT 2K2 aircraft intensive experiment, *Journal of Geophysical Research: Atmospheres*, 109, doi:10.1029/2004jd004960, 2004.
- 860 Roiger, A., Aufmhoff, H., Stock, P., Arnold, F., and Schlager, H.: An aircraft-borne chemical ionization - ion trap mass spectrometer (CI-ITMS) for fast PAN and PPN measurements, *Atmos. Meas. Tech.*, 4, 173-188, doi:10.5194/amt-4-173-2011, 2011.
- Samanta, B. R., Fernando, R., Rösch, D., Reisler, H., and Osborn, D. L.: Primary photodissociation mechanisms of pyruvic acid on S1: observation of methylhydroxycarbene and its chemical reaction in the gas phase, *Phys. Chem. Chem. Phys.*, 23, 4107-4119, doi:10.1039/D0CP06424F, 2021.
- 865 Sander, R., Baumgaertner, A., Cabrera-Perez, D., Frank, F., Gromov, S., Grooss, J. U., Harder, H., Huijnen, V., Jockel, P., Karydis, V. A., Niemeyer, K. E., Pozzer, A., Hella, R. B., Schultz, M. G., Taraborrelli, D., and Tauer, S.: The community

- atmospheric chemistry box model CAABA/MECCA-4.0, *Geoscientific Model Development*, 12, 1365-1385, doi:10.5194/gmd-12-1365-2019, 2019.
- 870 Shepson, P. B., Bottenheim, J. W., Hastie, D. R., and Venkatram, A.: Determination of the relative ozone and PAN deposition velocities at night, *Geophys. Res. Lett.*, 19, 1121-1124, doi:10.1029/92gl01118, 1992a.
- Shepson, P. B., Hastie, D. R., So, K. W., and Schiff, H. I.: Relationships between PAN, PPN and O₃ at urban and rural sites in ontario, *Atmos. Env. A*, 26, 1259-1270, doi:10.1016/0960-1686(92)90387-z, 1992b.
- 875 Sobanski, N., Schuladen, J., Schuster, G., Lelieveld, J., and Crowley, J. N.: A five-channel cavity ring-down spectrometer for the detection of NO₂, NO₃, N₂O₅, total peroxy nitrates and total alkyl nitrates, *Atmos. Meas. Tech.*, 9, 5103-5118, doi:10.5194/amt-9-5103-2016, 2016.
- Stefan, M. I., and Bolton, J. R.: Reinvestigation of the acetone degradation mechanism in dilute aqueous solution by the UV/H₂O₂ process, *Env. Sci. Tech.*, 33, 870-873, doi:10.1021/es9808548, 1999.
- 880 Talbot, R., Andreae, M., Berresheim, H., Jacob, D. J., and Beecher, K.: Sources and sinks of formic, acetic, and pyruvic acids over Central Amazonia: 2. Wet season, *Journal of Geophysical Research: Atmospheres*, 95, 16799-16811, doi:10.1029/JD095iD10p16799, 1990.
- Vesley, G. F., and Leermakers, P. A.: Photochemistry of alpha-keto acids + alpha-keto esters. 3. photolysis of pyruvic acid in vapor phase, *J. Phys. Chem.*, 68, 2364-2366, doi:10.1021/j100790a507, 1964.
- 885 Walker, D.: Pyruvate carboxylation and plant metabolism, *Biological Reviews*, 37, 215-254, doi:10.1111/j.1469-185X.1962.tb01611.x, 1962.
- Wang, N., Edtbauer, A., Stöner, C., Pozzer, A., Bourtsoukidis, E., Ernle, L., Dienhart, D., Hottmann, B., Fischer, H., Schuladen, J., Crowley, J. N., Paris, J. D., Lelieveld, J., and Williams, J.: Measurements of carbonyl compounds around the Arabian Peninsula indicate large missing sources of acetaldehyde, *Atmos. Chem. Phys. Discuss.*, 2020, 1-30, doi:10.5194/acp-2020-135, 2020.
- 890 Wang, S. Y., Hornbrook, R. S., Hills, A., Emmons, L. K., Tilmes, S., Lamarque, J. F., Jimenez, J. L., Campuzano-Jost, P., Nault, E. A., Crouse, J. D., Wennberg, P. O., Kim, M., Allen, H., Ryerson, T. B., Thompson, C. R., Peischl, J., Moore, F., Nance, D., Hall, B., Elkins, J., Tanner, D., Huey, L. G., Hall, S. R., Ullmann, K., Orlando, J. J., Tyndall, G. S., Flocke, F. M., Ray, E., Hanisco, T. F., Wolfe, G. M., St Clair, J., Commane, R., Daube, B., Barletta, B., Blake, D. R., Weinzierl, B., Dollner, M., Conley, A., Vitt, F., Wofsy, S. C., Riemer, D. D., and Apel, E. C.: Atmospheric acetaldehyde: importance of air-sea exchange and a missing source in the remote troposphere, *Geophys. Res. Lett.*, 46, 5601-5613, doi:10.1029/2019gl082034, 2019.
- Williams, J., Crowley, J., Fischer, H., Harder, H., Martinez, M., Petaja, T., Rinne, J., Back, J., Boy, M., Dal Maso, M., Hakala, J., Kajos, M., Keronen, P., Rantala, P., Aalto, J., Aaltonen, H., Paatero, J., Vesala, T., Hakola, H., Levula, J., Pohja, T., Herrmann, F., Auld, J., Mesarchaki, E., Song, W., Yassaa, N., Nolscher, A., Johnson, A. M., Custer, T., Sinha, V., Thieser, J., Pouvesle, N., Taraborrelli, D., Tang, M. J., Bozem, H., Hosaynali-Beygi, Z., Axinte, R., Oswald, R., Novelli, A., Kubistin, D., Hens, K., Javed, U., Trawny, K., Breitenberger, C., Hidalgo, P. J., Ebben, C. J., Geiger, F. M., Corrigan, A. L., Russell, L. M., Ouwersloot, H. G., de Arellano, J. V. G., Ganzeveld, L., Vogel, A., Beck, M., Bayerle, A., Kampf, C. J., Bertelmann, M., Kollner, F., Hoffmann, T., Valverde, J., Gonzalez, D., Riekkola, M. L., Kulmala, M., and Lelieveld, J.: The summertime Boreal forest field measurement intensive (HUMPPA-COPEC-2010): an overview of meteorological and chemical influences, *Atmos. Chem. Phys.*, 11, 10599-10618, doi:10.5194/acp-11-10599-2011, 2011.
- 905

Yamamoto, S., and Back, R. A.: The photolysis and thermal-decomposition of pyruvic-acid in the gas-phase, *Can. J. Chem.*, 63, 549-554, doi:10.1139/v85-089, 1985.

910

Table 1: Overview of different model scenarios for pyruvic acid.

Scenario	ϕ	α_1	α_2	α_3	β	Dominant products	$J_{\text{pyr}} [10^{-5} \text{s}^{-1}]$ (day/night)	$k_{\text{dep}} [10^{-5} \text{s}^{-1}]$ (day/night)	$k_{\text{total}} [10^{-5} \text{s}^{-1}]$ (day/night)	$E_{\text{pyr}}/E_{\text{MT}}$ (average)
A	0	—	—	—	—	—	0/0	9/18	9/18	0.58
B	0.20	0.6	0.35	0.05	+	CH_3CHO	3/0	9/18	12/18	0.62
C	0.84	0.95	0	0.05	0.05	$\text{HO}_2 + \text{CH}_3\text{CO}_3$	12/0	9/18	21/18	0.74

ϕ = photolysis quantum yield, α_i and β are branching ratios forming the dominant products. k_i are loss rates of pyruvic acid, $E_{\text{pyr}}/E_{\text{MT}}$ is the emission rate of pyruvic acid relative to MT.

915

Table 12: Emission rate of pyruvic acid (E_{pyr}) relative to isoprene (E_{iso}) and MT (E_{MT}), derived from different field and enclosure studies.

Reference	Location	Plant species	$(E_{\text{pyr}} / E_{\text{iso}})$	$(E_{\text{pyr}} / E_{\text{MT}})$
This study	Hyytiälä, Finland	Boreal forest	~ 20	0.62
Talbot et al. (1990)	Manaus, Brazil	Tropical forest	0.003	-
Jardine et al. (2010b)	Biosphere 2, Arizona, US	Tropical biome	0.17	4
Jardine et al. (2010b)	Biosphere 2, Arizona, US	Mango tree	0.05	1.7
Jardine et al. (2010a)	Biosphere 2, Arizona, US	Creosotebush	0.05	0.07

920

Table 2. Theory-predicted high-pressure rate coefficients for reaction of singlet CH₃COH

Reactants	Products	<i>k</i> (298 K)	<i>A</i>	<i>n</i>	<i>E_a</i>
<i>syn</i> -CH ₃ COH + O ₂	CH ₃ C(OH)OO [•]	2.2×10 ⁻²⁰	5.74E-22	3.05	4092
<i>anti</i> -CH ₃ COH + O ₂	CH ₃ C(OH)OO [•]	6.6×10 ⁻²¹	1.71E-22	2.97	3960
<i>syn</i> -CH ₃ COH + H ₂ O	CH ₃ CH(OH) ₂	1.9×10 ⁻²⁰	1.57E-55	13.56	-1049
<i>anti</i> -CH ₃ COH + H ₂ O	CH ₃ CH(OH) ₂	5.7×10 ⁻²¹	1.09E-61	15.61	-1443
<i>syn</i> -CH ₃ COH	<i>anti</i> -CH ₃ COH	8.9×10 ⁻³	7.86E-20	10.77	6598
	CH ₂ =CHOH	1.9×10 ⁻⁴	3.62E-91	34.20	-1444
	<i>anti</i> -CH ₃ COH	2.8×10 ⁻⁵	6.55E-20	10.71	8137
<i>anti</i> -CH ₃ COH	<i>syn</i> -CH ₃ COH	2.8×10 ⁻⁵	6.55E-20	10.71	8137
	CH ₂ =CHOH	9.2×10 ⁻⁵	2.02E-114	40.40	-6660
	CH ₃ C(=O)H	3.4×10 ⁻⁴	1.26E-81	30.96	-563
CH ₂ =CHOH + HCOOH	CH ₃ C(=O)H + HCOOH	3.3×10 ⁻²⁵	1.82E-76	19.88	-1426
CH ₃ C(=O)H + HCOOH	CH ₂ =CHOH + HCOOH	8.1×10 ⁻²⁷	1.09E-78	20.59	-633

925

Calculations were performed at the CCSD(T)//M06-2X-D3 with MC-TST level of theory. Rate coefficient are given at 298 K (s⁻¹ or cm³ molecule⁻¹ s⁻¹). Temperature dependent rate coefficients can be calculated using the parameters of a Kooij expression $k(200-450\text{ K}) = A \times (T/K)^n \times \exp(-E_a/T)$ with *A* in s⁻¹ or cm³ molecule⁻¹ s⁻¹ and *E_a* in K.

930

Scenario	Production rate in IBAIRN [10 ⁵ -molecule-cm ⁻³ -s ⁻¹]			Production rate in HUMPPA [10 ⁵ -molecule-cm ⁻³ -s ⁻¹]		
	A	B	C	A	B	C
OH	13.1	13.3	14.8	43.9	44.4	47.6
HO ₂	5.8	5.9	7.9	34.7	35.6	41.7
CH ₃ CO ₂	1.2	1.2	2.2	17.3	17.9	21.6
CH ₃ CHO	-	-	-	0.1	1.1	0.3
CH ₃ O ₂	1.2	1.2	1.7	4.7	4.9	6.0

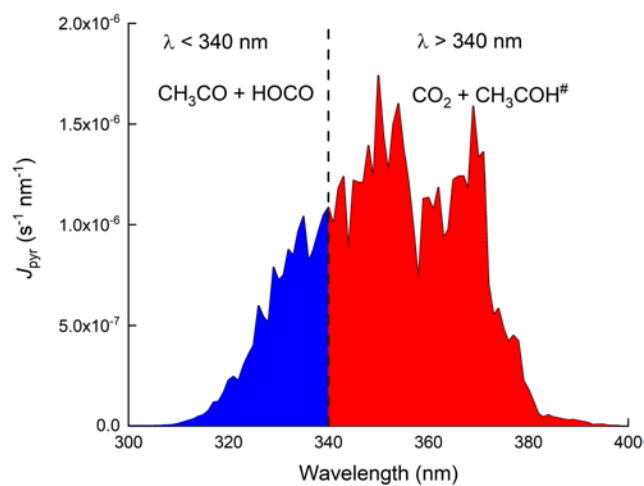
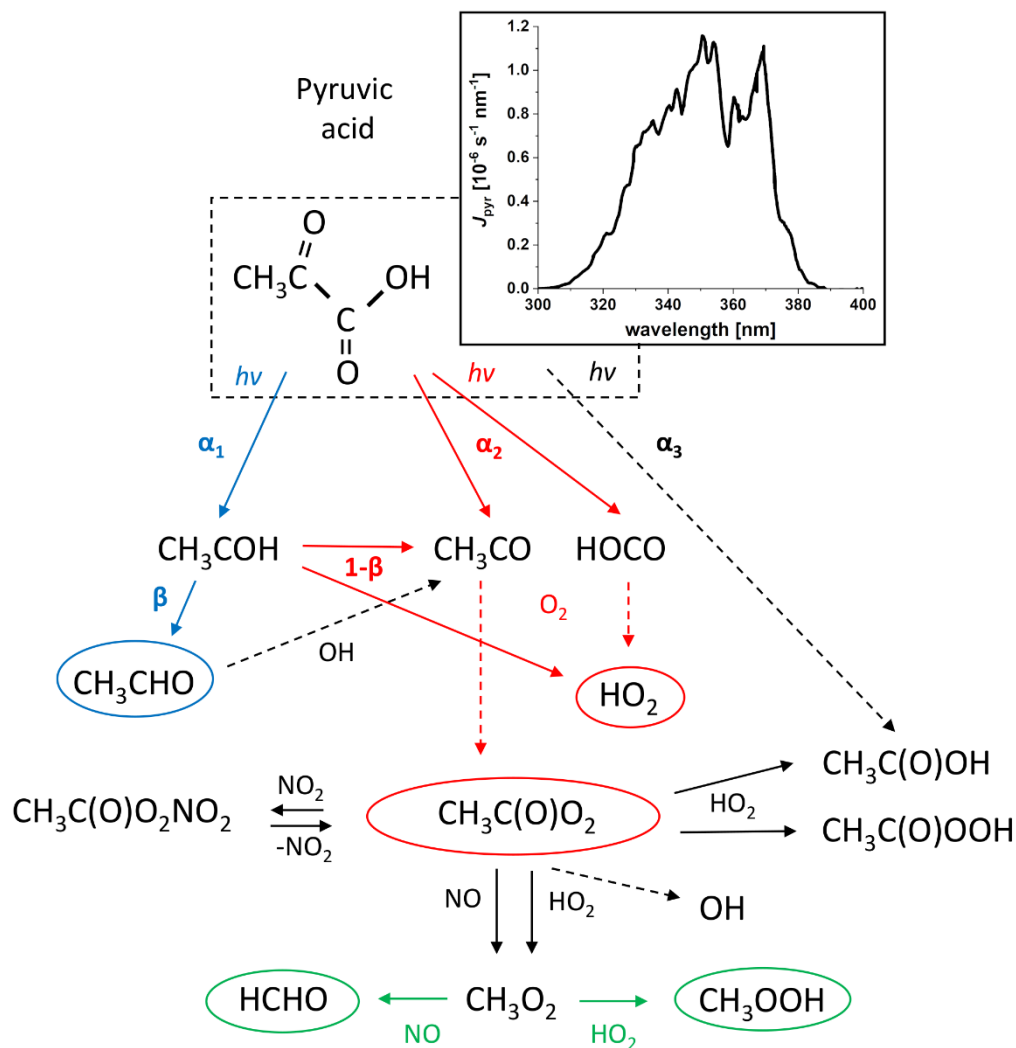


Figure 1: Wavelength resolved photolysis rates (J_{pyr}) for 13.09.2016 at solar noon. J_{pyr} was calculated using a photolysis quantum yield of 1 and the absorption cross sections at 298 K preferred by IUPAC (2020).



945 **Figure 1:** Radical and stable products from the photolysis of pyruvic acid (including branching ratios α_i and β) along with the wavelength resolved photolysis rates (J_{pyr} in units of $10^{-6} \text{ s}^{-1} \text{ nm}^{-1}$) for 13.09.2016 at solar noon. J_{pyr} was calculated using a photolysis quantum yield of $\phi=0.2$ and the absorption cross sections at 298 K preferred by IUPAC (2020).

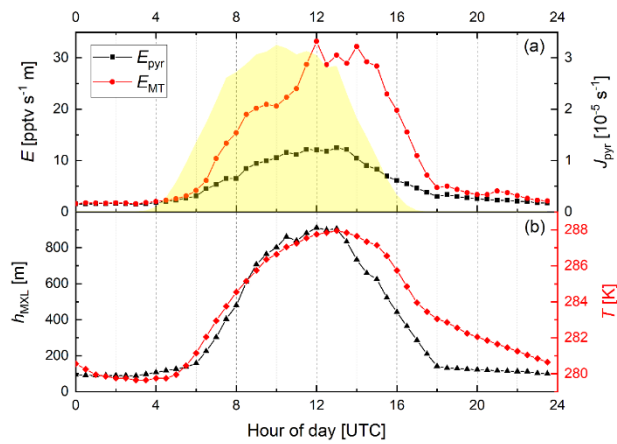


Figure 2: Diel variation of the (MXL height-corrected) emission rates of pyruvic acid (E_{pyr} , scenario B) and monoterpenes (E_{MT}) along with J_{pyr} (yellow shaded)

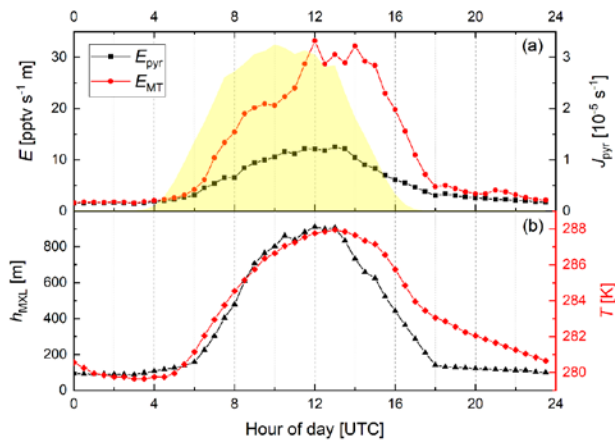


Figure 2: Diel variation of the (MXL height-corrected) emission rates of pyruvic acid (E_{pyr} , scenario B) and monoterpenes (E_{MT}) along with J_{pyr} (yellow shaded), T and h_{MXL} for the IBairn campaign.

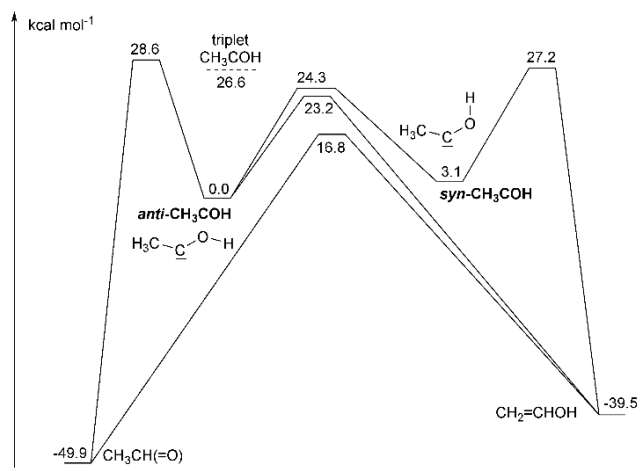


Figure 3: ZPE-corrected potential energy surface for unimolecular reactions of singlet CH₃COH at the CCSD(T)//M06-2X-D3 level of theory.

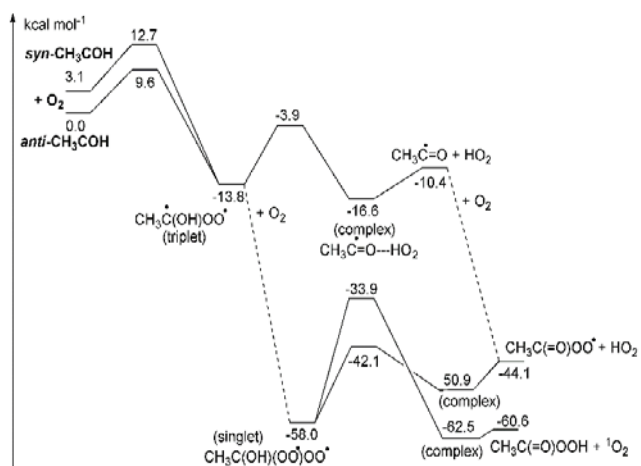


Figure 4: ZPE-corrected potential energy surface for reaction of singlet CH_3COH with O_2 at the CCSD(T)//M06-2X-D3 level of theory.

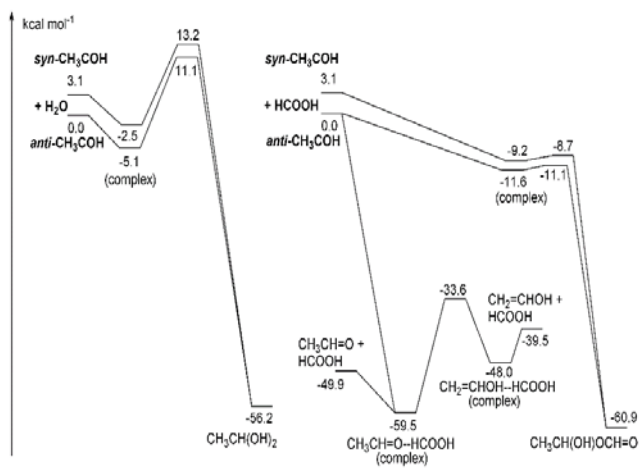


Figure 5: ZPE-corrected potential energy surface for reactions of singlet CH_3COH with H_2O (left) and HCOOH (right) at the CCSD(T)//M06-2X-D3 level of theory.

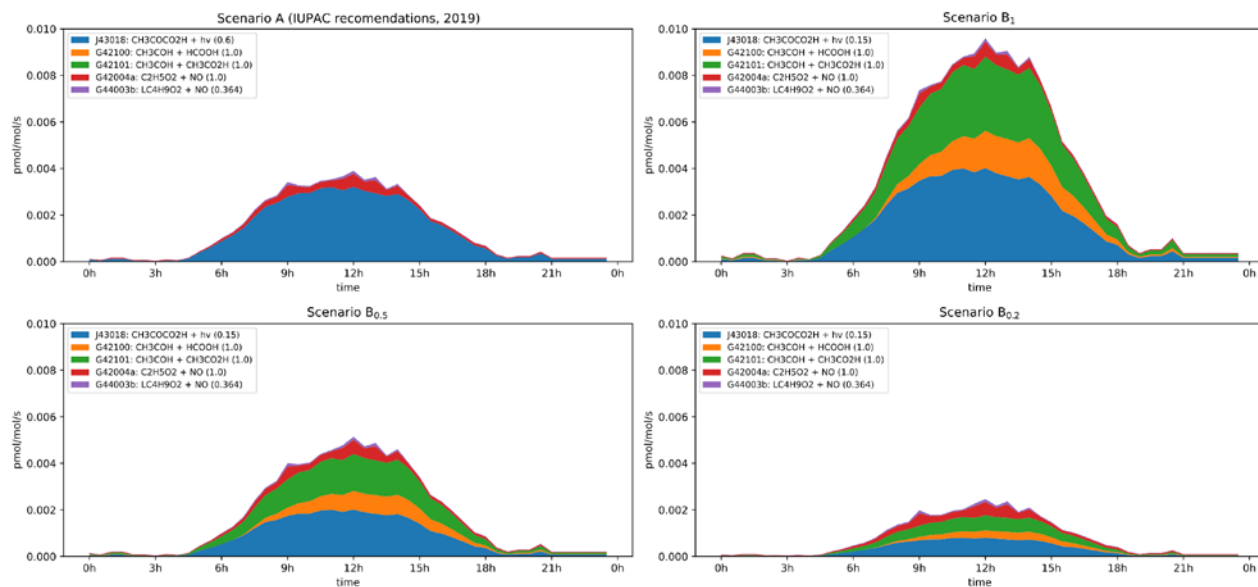


Figure 6: Modelled rates of CH_3CHO formation (in ppt per seconds) through the diel cycle from photolysis of pyruvic acid (blue, orange and green) and other reactions during IBAIRN. Top left: Scenario A (IUPAC recommendations from 2019). Top right: Scenario B₁. Bottom left: Scenario B_{0.5}. Bottom right: Scenario B_{0.2}. In the legend, the first term is the equation tag used by CAABA/MECCA for the reaction. LC₄H₉O₂ is the peroxy radical formed in the reaction of OH with butane. A full listing of the reactions can be downloaded (see “data availability”).

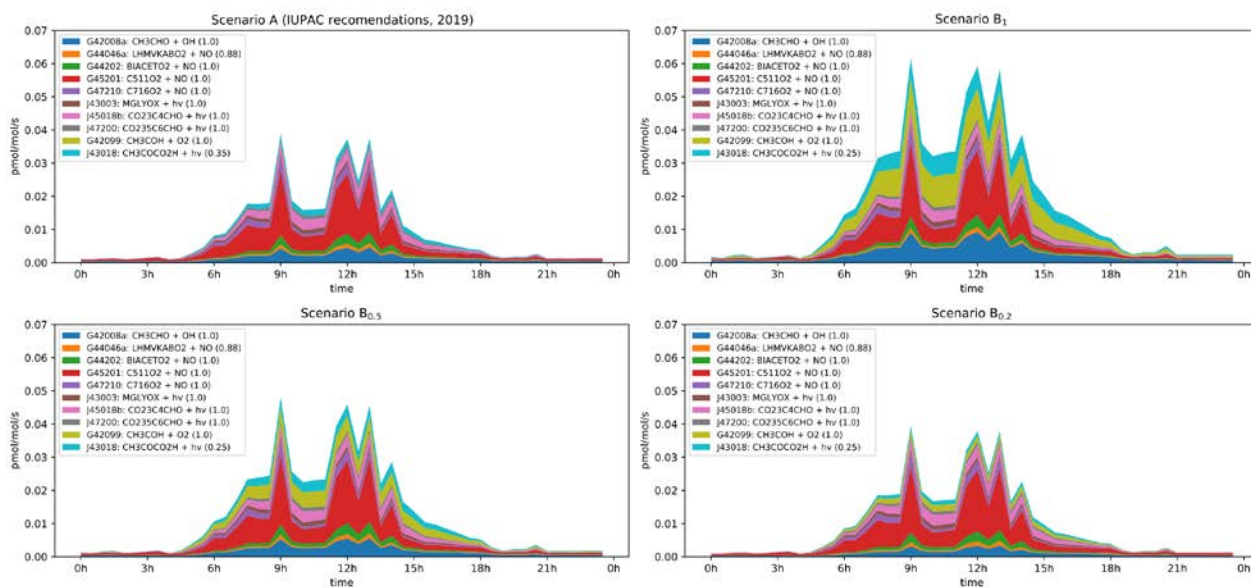


Figure 7: Modelled rates of CH_3CO formation (in ppt per seconds) through the diel cycle from photolysis of pyruvic acid (blue, orange and green) and other photochemical processes during IBAIRN. Top left: Scenario A (IUPAC recommendations from 2019). Top right: Scenario B₁. Bottom left: Scenario B_{0.5}. Bottom right: Scenario B_{0.2}. In the legend, the first term is the equation tag used by CAABA/MECCA for the reaction. A full listing of the reactions can be downloaded (see “data availability”).

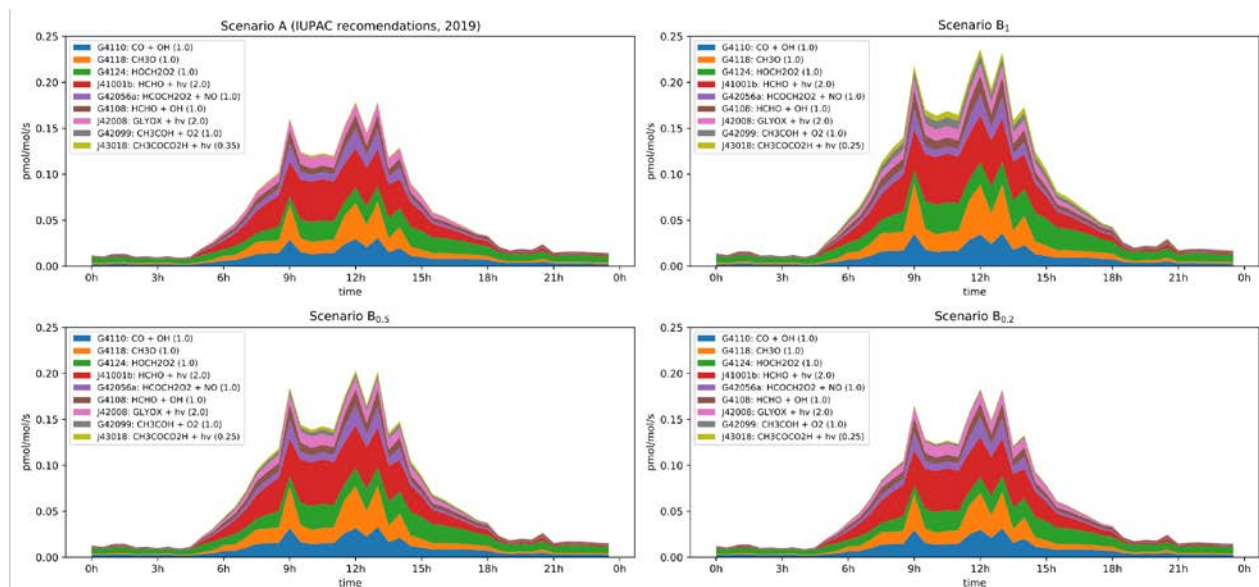
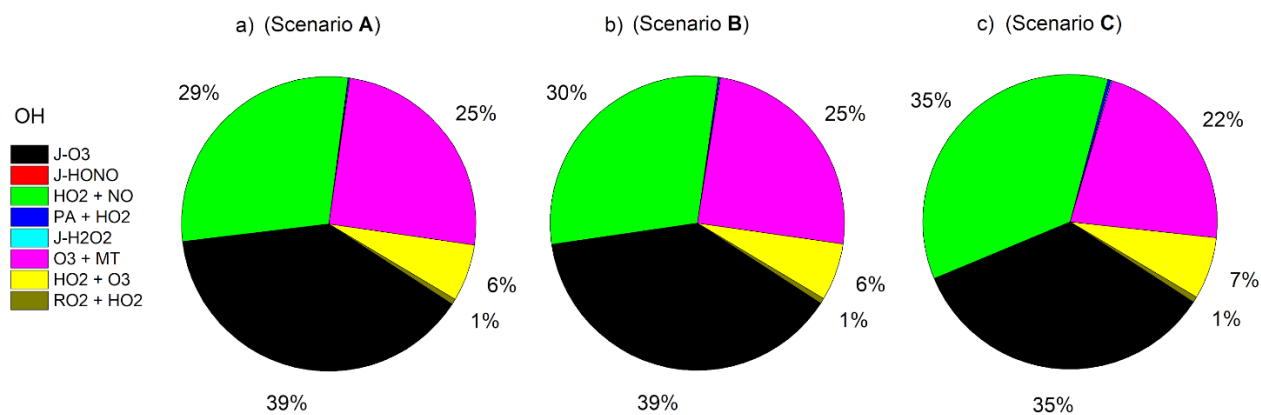


Figure 8: Modelled rates of HO₂ formation (in ppt per seconds) through the diel cycle from photolysis of pyruvic acid (blue, orange and green) and other photochemical processes during IBAIRN. Top left: Scenario A (IUPAC recommendations from 2019). Top right: Scenario B₁. Bottom left: Scenario B_{0.5}. Bottom right: Scenario B_{0.2}. In the legend, the first term is the MCM designation for the reaction. A full listing of the reactions can be downloaded (see “data availability”).



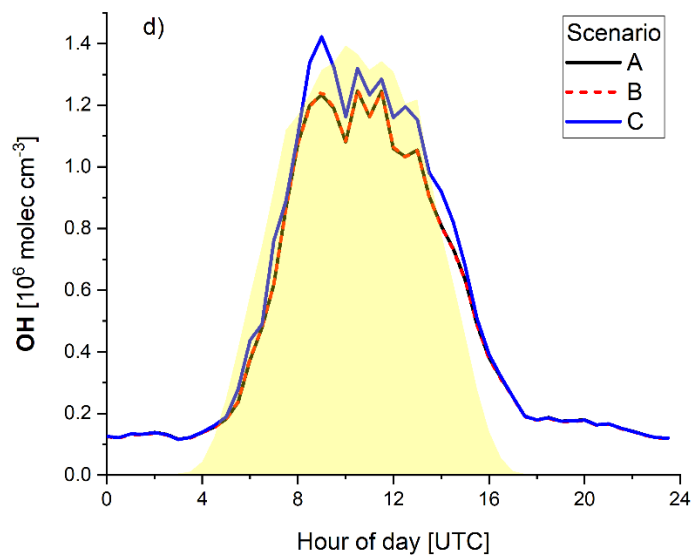


Figure 3: Modelled relative source strength (averaged throughout the diel cycle) and concentration of OH (along with the relative photolysis rate J_{pyr} in yellow) during IBAIRN using scenarios A, B and C (Table 1). J = photolysis; PA = peroxyacetyl radical; MT = sum of monoterpenes.

975

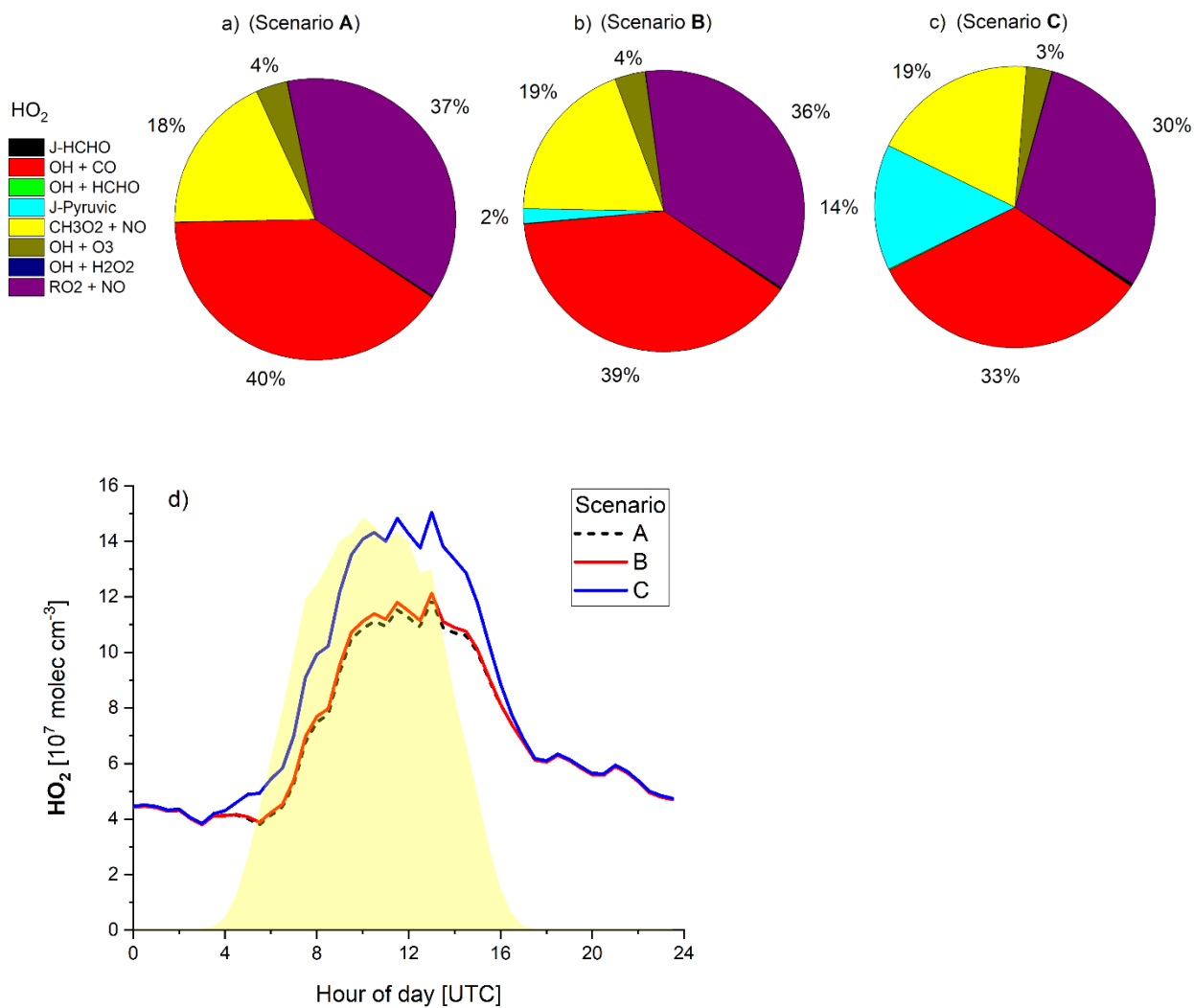


Figure 4: Modelled relative source strength (averaged throughout the diel cycle) and concentration of HO₂ (along with the relative photolysis rate J_{pyr} in yellow) during IBAIRN using scenarios A, B and C.

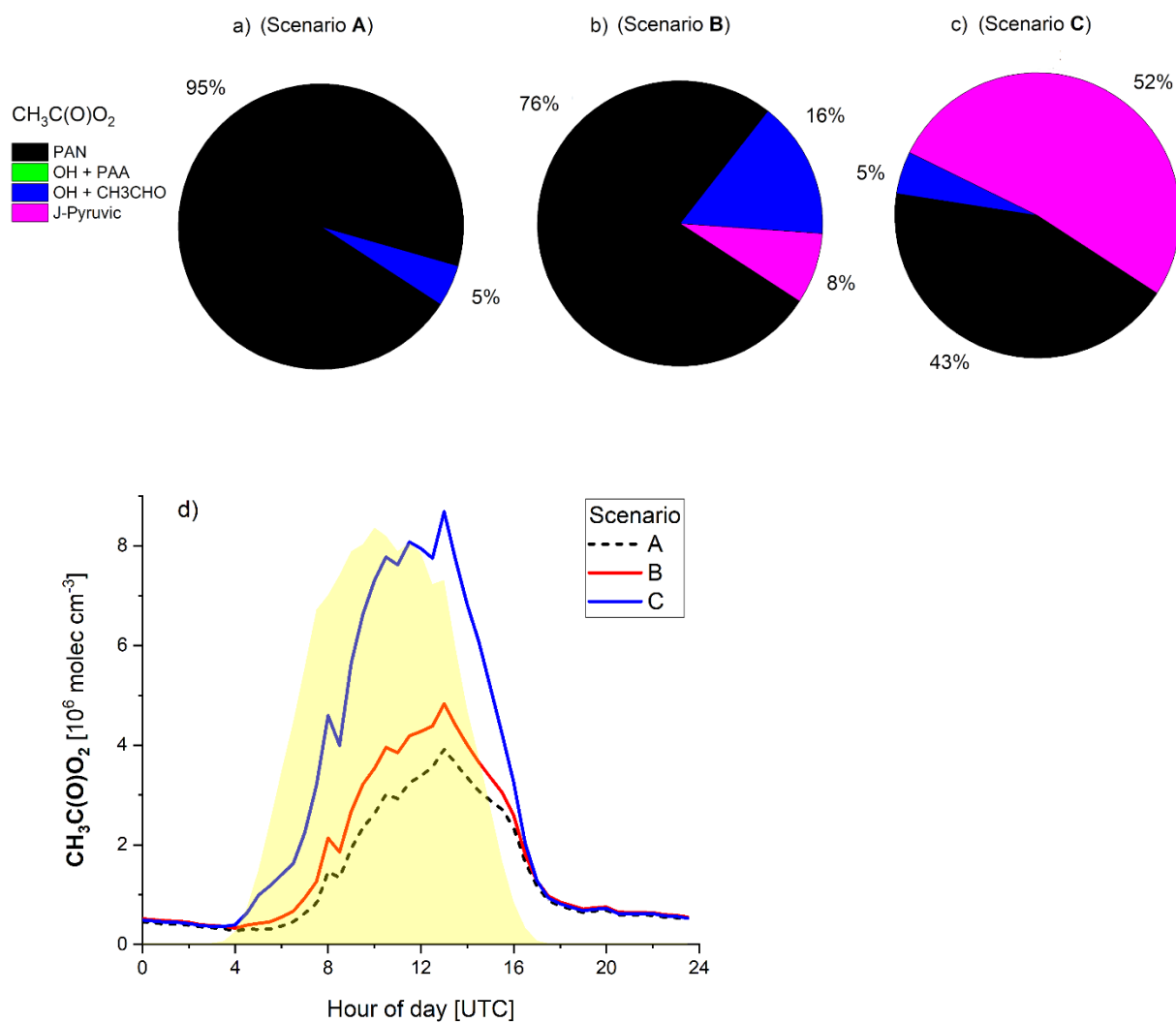


Figure 5: Modelled relative source strength (averaged throughout the diel cycle) and concentration of $\text{CH}_3\text{C}(\text{O})\text{O}_2$ (along with the relative photolysis rate J_{pyr} in yellow) during IB AIRN using scenarios A, B and C.

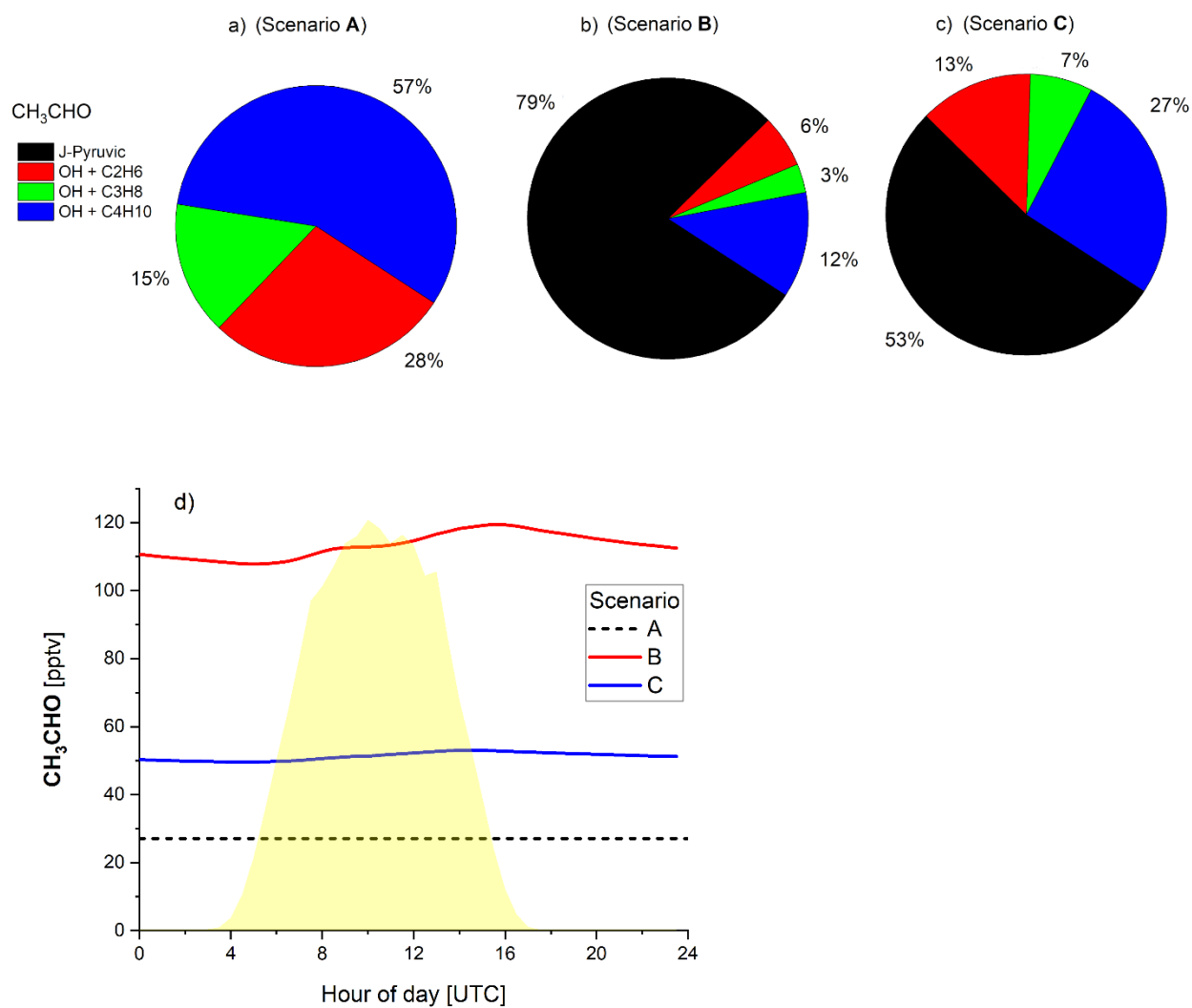


Figure 6: Modelled relative source strength (averaged throughout the diel cycle) and concentration of CH₃CHO (along with the relative photolysis rate J_{pyr} in yellow) during IBAIRN using scenarios A, B and C.

995

1000

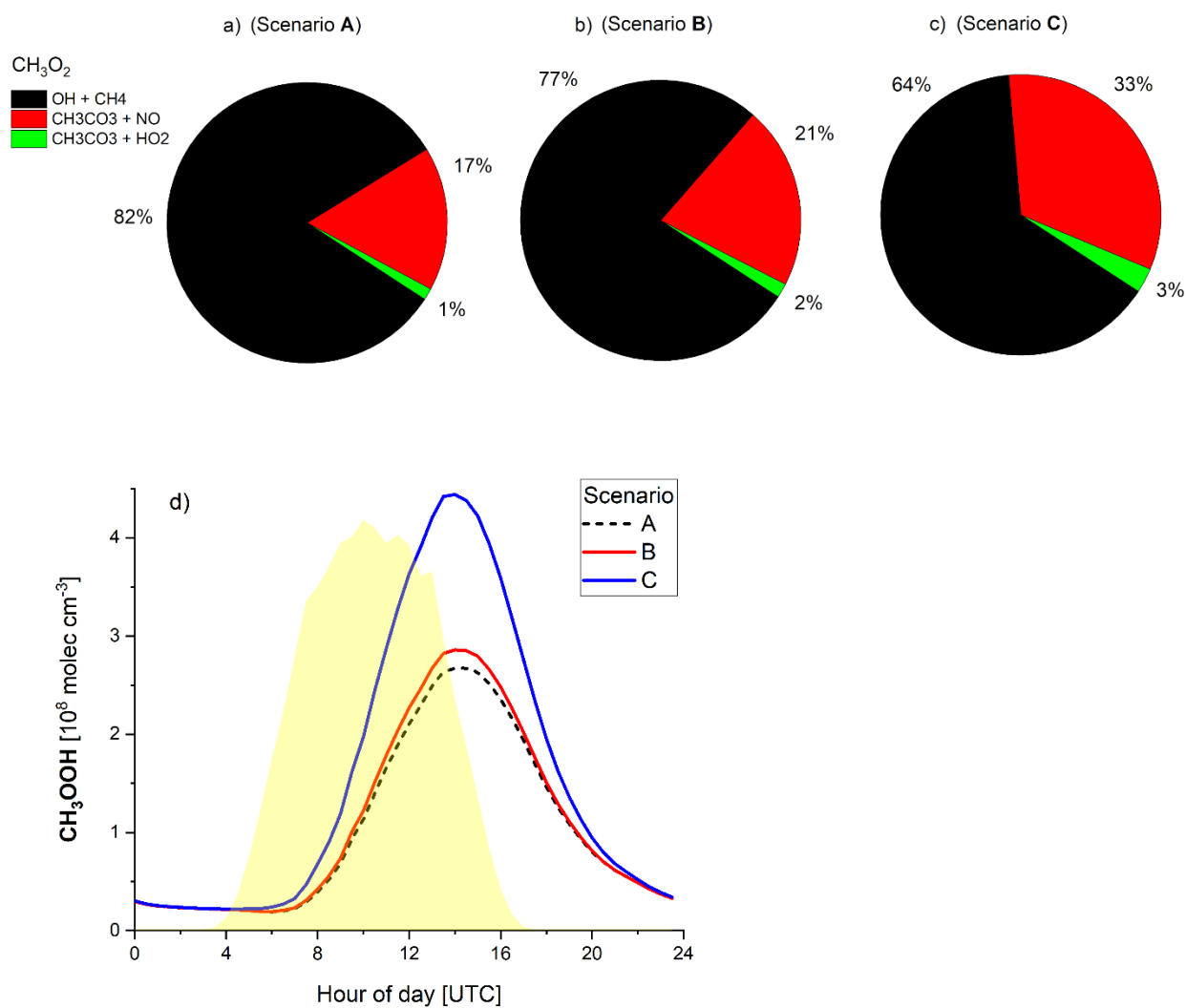


Figure 7: Modelled relative source strength (averaged throughout the diel cycle) of CH_3O_2 and concentration of CH_3OOH (along with the relative photolysis rate J_{pyr} in yellow) during IBairn using scenarios A, B and C.

1005

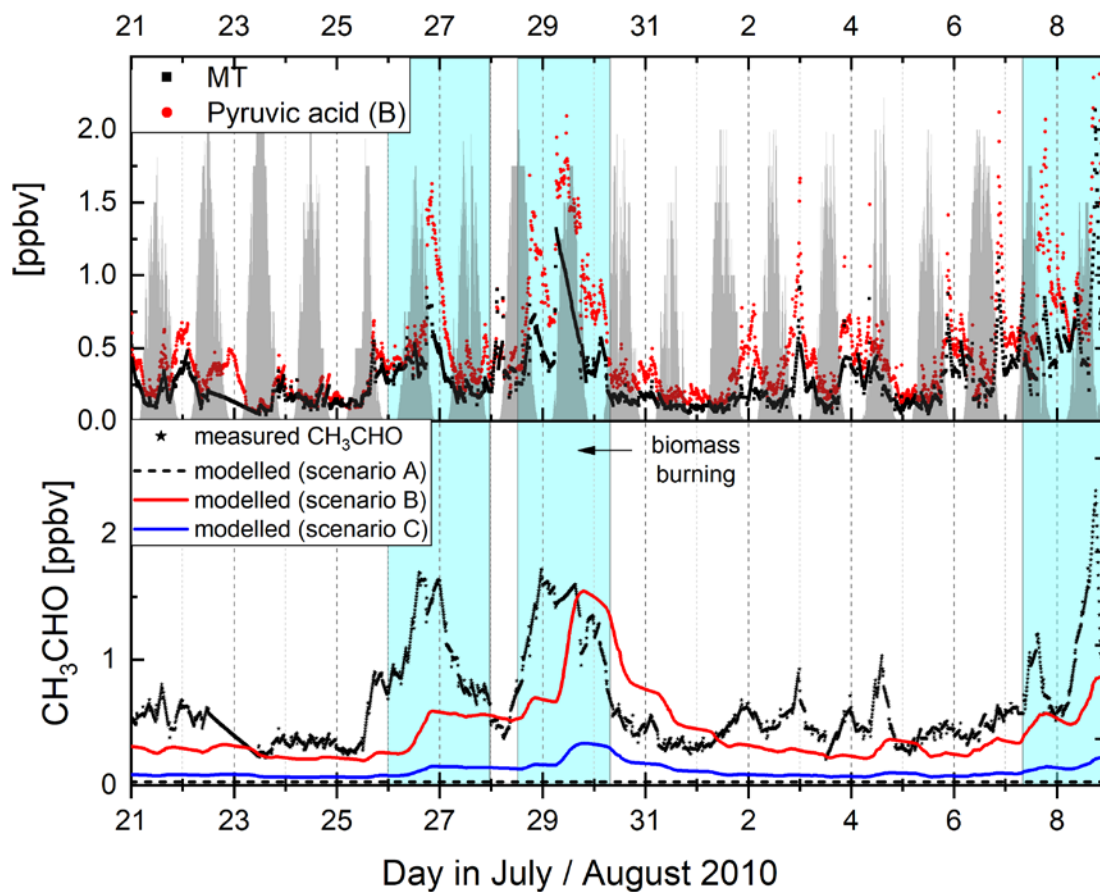
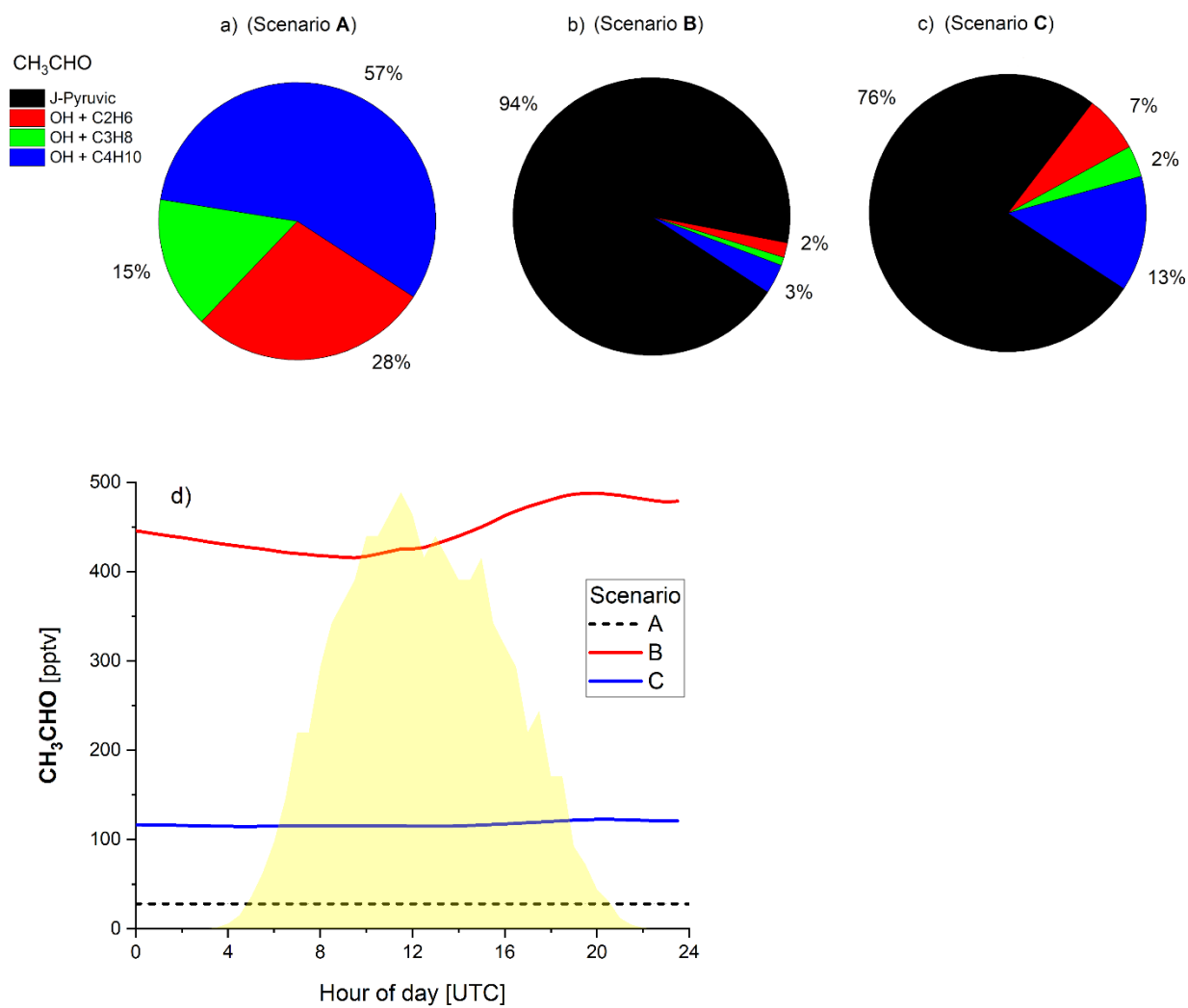


Figure 8: Upper panel: mixing ratio of MT (measured) and pyruvic acid (modelled, scenario B) during HUMPPA along with the photolysis rate J_{pyr} in grey. Lower panel: measured and modelled (scenarios A, B and C) acetaldehyde mixing ratios. Periods impacted by biomass burning plumes are highlighted in light blue.



1020

Figure 9: Modelled relative source strength (averaged throughout the diel cycle) and concentration of CH₃CHO during HUMPPA using scenarios A, B and C.

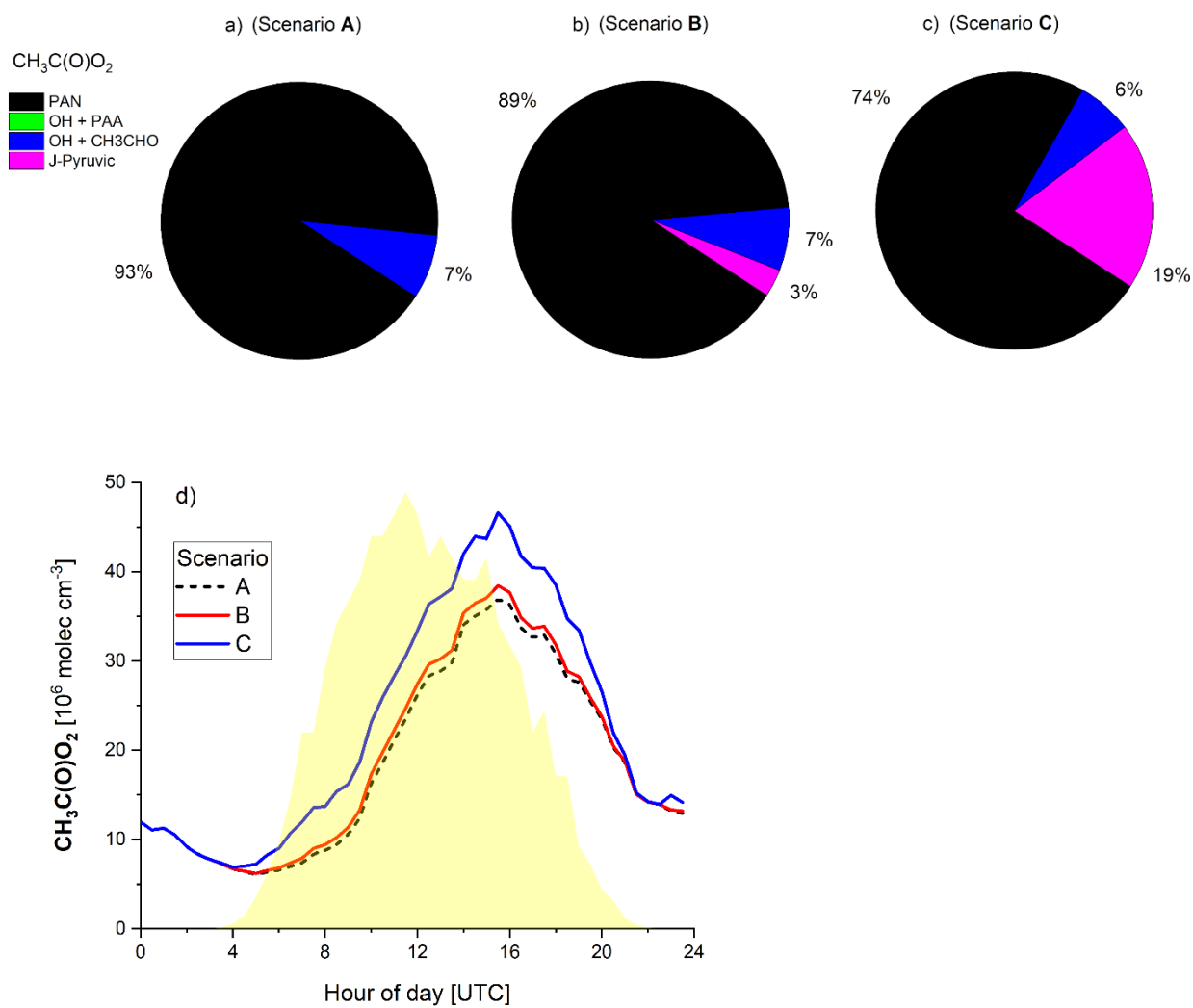


Figure 10: Modelled relative source strength (averaged throughout the diel cycle) and concentration of CH₃C(O)O₂ (along with the relative photolysis rate J_{pyr} in yellow) during HUMPPA using scenarios A, B and C.